Multi-layered chromatin proteomics identifies cell vulnerabilities in DNA repair

Gianluca Sigismondo [ID][1], **Lavinia Arseni**[2], **Nicolàs Palacio-Escat**[1], **Thomas G Hofmann** [ID][3], **Martina Seiffert**[2] and **Jeroen Krijgsveld**[1,4,*]

[1]Division of Proteomics of Stem Cells and Cancer, German Cancer Research Center (DKFZ), 69120 Heidelberg, Germany, [2]Division of Molecular Genetics, German Cancer Research Center (DKFZ), 69120 Heidelberg, Germany, [3]Institute of Toxicology, University Medical Center of the Johannes Gutenberg University Mainz, 55131 Mainz, Germany and [4]Medical Faculty, Heidelberg University, 69120 Heidelberg, Germany

ABSTRACT

The DNA damage response (DDR) is essential to maintain genome stability, and its deregulation predisposes to carcinogenesis while encompassing attractive targets for cancer therapy. Chromatin governs the DDR via the concerted interplay among different layers, including DNA, histone post-translational modifications (hPTMs) and chromatin-associated proteins. Here, we employ multi-layered proteomics to characterize chromatin-mediated functional interactions of repair proteins, signatures of hPTMs and the DNA-bound proteome during DNA double-strand break (DSB) repair at high temporal resolution. Our data illuminate the dynamics of known and novel DDR-associated factors both at chromatin and at DSBs. We functionally attribute novel chromatin-associated proteins to repair by non-homologous end-joining (NHEJ), homologous recombination (HR) and DSB repair pathway choice. We reveal histone reader ATAD2, microtubule organizer TPX2 and histone methyltransferase G9A as regulators of HR and involved in poly-ADP-ribose polymerase-inhibitor sensitivity. Furthermore, we distinguish hPTMs that are globally induced by DNA damage from those specifically acquired at sites flanking DSBs (γH2AX foci-specific) and profiled their dynamics during the DDR. Integration of complementary chromatin layers implicates G9A-mediated monomethylation of H3K56 in DSBs repair via HR. Our data provide a dynamic chromatin-centered view of the DDR that can be further mined to identify novel mechanistic links and cell vulnerabilities in DSB repair.

GRAPHICAL ABSTRACT
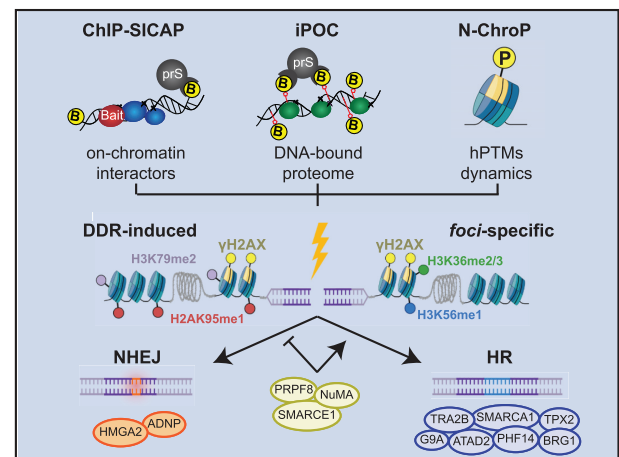
INTRODUCTION

DNA damage represents a major risk for genome stability, and among the different types of lesions, double-strand breaks (DSBs) are the most detrimental; indeed if not properly repaired these lesions predispose to DNA mutations and loss of genomic information. To prevent genome instability, two main repair mechanisms have evolved: the error-prone non-homologous end joining (NHEJ) based on the fast ligation of the damaged site and the homologous-directed recombination (HDR or HR), where sister chromatid is used as template for error-free DSB repair ([1–4]). Notably, the DNA damage repair occurs in the context of chromatin, a higher-ordered structure composed of DNA wrapped around histone proteins and stabilized by non-histone components ([5]). Upon DSB formation, chromatin determinants reorganize the structure surrounding the lesion, activate a specific signaling cascade and recruit the repair machinery for efficient DSB resolution via either NHEJ or HR ([6]). In particular, the sensor complex com-

posed of MRE11, RAD50 and NBN (Nbs1) (MRN complex) rapidly accumulates at damaged sites where it promotes the Ataxia telangiectasia mutated (ATM)-mediated phosphorylation of the histone variant H2A.X (referred to as γH2AX). This histone post-translational modification (hPTM) thus marks DSBs and acts as a docking site for the recruitment of Mediator of DNA damage checkpoint protein 1 (MDC1) and TP53BP1/53BP1. The latter, together with the XRCC6-XRCC5 (Ku70/80) proteins and the Rap1-interacting factor 1 (RIF1)-shieldin complex, is responsible for protection of the break sites against end-resection and thereby guides repair pathway choice towards NHEJ. The MRN complex plays a pivotal role as it also facilitates extensive end-resection in complex with BRCA1, CtIP and EXO1, thus creating single-stranded DNA (ss-DNA) filaments rapidly stabilized by the replication factor RNA polymerase I subunit A1 (RPA1). Breast cancer type 1 susceptibility protein (BRCA1) recruits the Partner and localizer of BRCA2 (PALB2-BRCA2) complex, which loads RAD51 to initiate sister-chromatid strand invasion and DSB repair via HR (7,8).

Because of their central role in cell survival, proteins participating in the DDR are often de-regulated in different types of cancers; interestingly, some loss-of-function mutations represent innovative therapeutic opportunities. The best studied example is BRCA1 deregulation in ovarian and breast cancer, which results in the accumulation of mutations and predisposes to genomic instability (9), while acquiring extreme sensitivity to inhibitors of poly-ADP-ribose polymerase (PARPi). Indeed, in an HR-deficient background DSB repair largely relies on NHEJ, which requires PARP activity (10). In consequence, PARPi treatment in HR-deficient cells triggers efficient and selective cancer cell death, as more recently exploited in cancer therapy. For this reason, genomic screens are broadly employed to identify synthetic lethality with drugs such as PARPi. Nevertheless, patients often develop drug resistance, thus indicating the need for a deeper characterization of the repair process to rationally propose alternative drug targets.

In light of this, in the past decades the core components of DSB repair pathways have been intensively studied (11–14); however, it is only partially understood how these machineries are functionally embedded in the broader chromatin context, and how chromatin determinants impinge on repair pathway choice (15). Beyond γH2AX, the role of other hPTMs in DDR has come into focus (16), either by regulating DNA accessibility and chromatin stiffness (17–20) or by acting as docking sites for the recruitment of DSB repair proteins (21–24). As a consequence, the more accredited models for the DSB repair rely on the coordinated action of determinants belonging to different chromatin layers, including DNA, hPTMs, components of the DDR machineries and chromatin-associated proteins, to harmoniously ensure successful DSB repair. In spite of that, how these determinants are functionally connected, and how they are dynamically and temporally regulated upon induction of DSBs, are major questions that remain to be addressed. The high complexity of the DDR suggests that no single approach is sufficient to capture the regulation of this fundamental biological process. Therefore, here, we bring together the unbiased nature of mass

spectrometry with three complementary strategies to study DSB-induced chromatin dynamics at different scales of resolution, namely (i) chromatin-wide, by investigating the DNA-bound proteome (iPOC), (ii) targeted, by identifying functional interactors of known DDR proteins (ChIP-SICAP) (25,26) and (iii) at the level of mono-nucleosomes, to determine hPTM kinetics (N-ChroP) (27,28). Moreover, we added a temporal dimension to the study in order to characterize the DDR process from a chromatin-centered perspective in unprecedented detail and with high temporal resolution. In addition, we validated proteomic data by means of orthogonal functional assays, thus assigning a role of 12 newly identified candidates in the regulation of NHEJ, HR or repair pathway choice. Moreover, we show that depletion of novel HR-regulating proteins (i.e. G9A, ATAD2, TPX2) is synthetic lethal with PARPi. Finally, overlay of these complementary proteomic layers allowed us to reconstruct potential cause–effect mechanisms between DSB-mediated chromatin recruitment and epigenetic regulation during DNA repair. An elective example is represented by the chromatin recruitment of the methyltransferase G9A followed by the monomethylation of its substrate H3K56 specifically at foci-specific mononucleosomes marked by γH2AX, thus implying a role for this hPTM in DSB repair. Collectively, beyond providing deep insight into DSB-mediated chromatin dynamics, our approach identifies novel cell vulnerabilities as leads for the development of potential therapeutic interventions. Finally, to facilitate further exploration of chromatin dynamics during the DDR, we make our data available as a resource at https://chromatin-proteomics.dkfz.de/.

MATERIALS AND METHODS
Biological resources

U2OS (ATCC) and U2OS-ID3-GFP (kindly provided by Dr Ali Bakr, DKFZ, Heidelberg) cell lines were cultured in Dulbecco's modified Eagle's medium (DMEM) supplemented with antibiotics, and 10% FCS (Invitrogen) at 37°C under a humidified atmosphere with 5% CO_2. U2OS-TLR cells (kindly provided by Prof. Ayoub N) were cultured as U2OS with puromycin 0.6 μg/ml. U2OS pIRES-mCherry-m53BP1 (kindly provided by Prof. Randi Syljuåsen, Oslo University Hospital) and AID-DIvA (MTA with Dr Gaelle Legube, CBI, Toulouse) were cultured as U2OS with 800 μg/ml G418, Geneticin (Thermo Fisher Scientific, 10131035). DSB were induced in AID-DIvA with 300 nM hydroxyl tamoxifen (Sigma-Aldrich, H6278) for 4 h. Repair was promoted with 500 μg/ml Auxin (indole-3-acetic acid sodium salt, Sigma-Aldrich, I5148) for 1 h.

Chromatin-associated interactors investigated through ChIP-SICAP

ChIP-SICAP experiments were performed as described before (25) with some modifications. In brief, U2OS cells were metabolically labeled in SILAC (29) DMEM medium containing light (Arg0, Lys0), medium (Arg6, Lys4) or heavy (Arg10, Lys8) amino acids. For experimental design related to Figure 1, U2OS cell pellets corresponding to 24×10^6 cells were cross-linked with formaldehyde (1% final concentration) in the absence (medium) or after 1 h recovery from
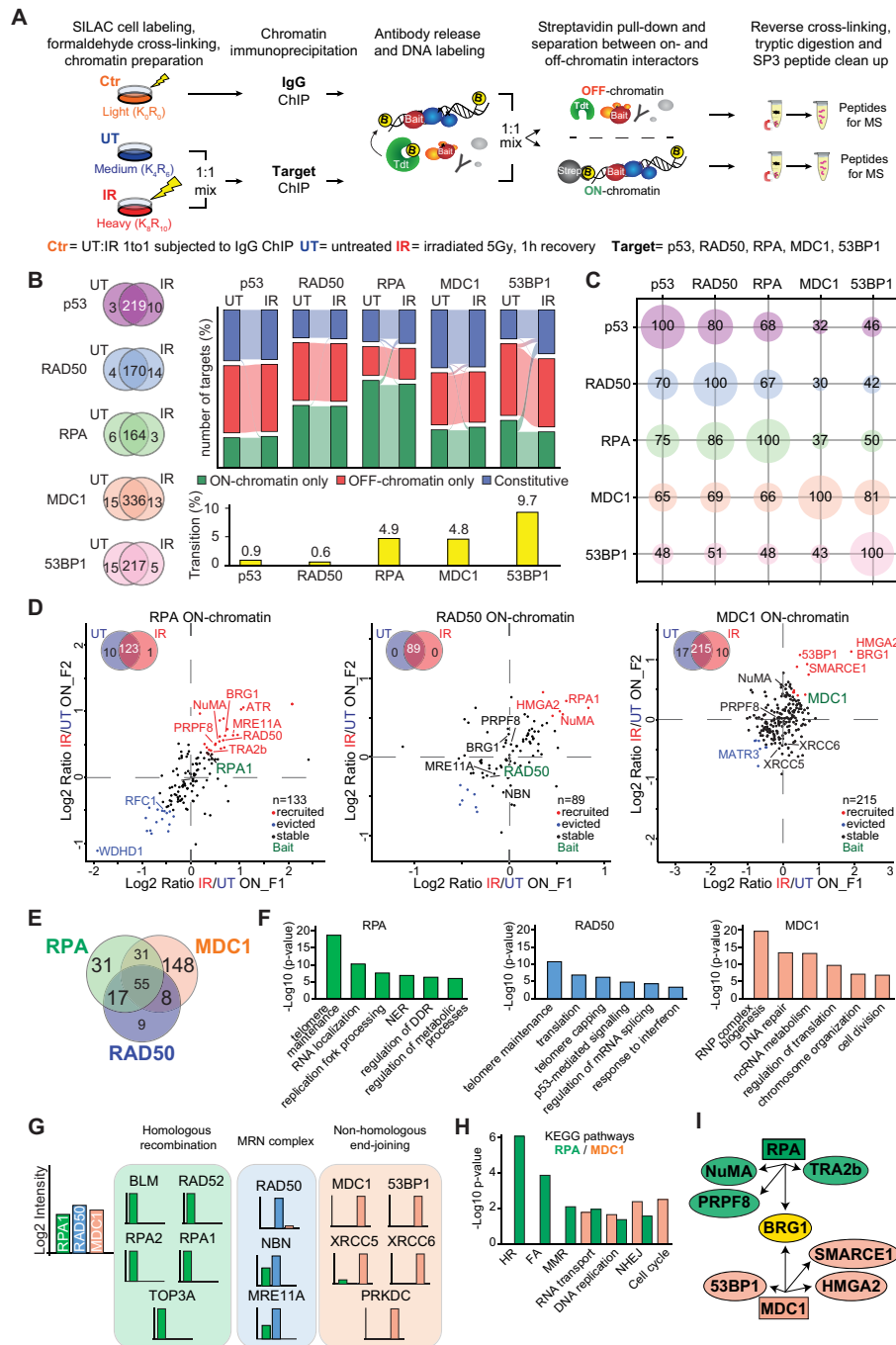
Figure 1. On-chromatin functional interactors of DDR core components. (**A**) ChIP-SICAP experimental strategy. Crosslinked chromatin preparation from SILAC labeled cells were enriched for target DDR proteins in the absence (UT) or upon DSB (IR) followed by quantification of functional interactors of the bait while in its ON- or OFF-chromatin state. IgG enrichment serves as internal technical control. (**B**) Venn diagrams show the overlap of binders between untreated condition (UT) and upon ionizing radiations (IR). Sankey diagrams represent the IR-mediated dynamics of functional interactors for protein used as bait in (A); proteins in common between UT and IR were classified into constitutively associated with the target (constitutive) or quantified exclusively in the ON- and OFF-chromatin fraction (ON- and OFF-only, respectively). Bar plots represent the percentage of candidates changing association with the bait between UT and IR condition (i.e. transition), (**C**) Bubble charts display the frequency of intersection (expressed as percentage) between interactors of the different proteins used as bait in ChIP-SICAP. The circle size represents the percentage of the overlap. (**D**) Scatterplots representing modulation of ON-chromatin interactors recruited (red) or evicted (blue) from RPA, RAD50, or MDC1 sites upon DSB (IR) in comparison with untreated condition (UT). Venn diagrams show the number of ON-chromatin interactors quantified in each experiment. (**E**) Intersection among the ON-chromatin interactors quantified in RPA, RAD50 or MDC1 experiment. (**F**) Top-6 gene ontology categories associated with ON-chromatin interactors quantified in RPA, RAD50 or MDC1 ChIP-SICAP. (**G**) Log2 intensity of proteins belonging to HR, MRN complex, or NHEJ and enriched in RPA1 (green), RAD50 (blue) and MDC1 (orange) ChIP-SICAP. (**H**) KEGG pathways associated with proteins functionally interacting with RPA (green) or MDC1 (orange), expressed as difference between *P*-value in RPA and MDC1 (in -log10). (**I**) Cartoon representing candidate proteins associated with RPA (green), MDC1 (orange) or both targets (yellow) upon DSB formation. Squares and elliptical shapes correspond to proteins used as bait in ChIP-SICAP, and their DSB-induced interactors, respectively.

Table 1. Reagents used in this study

Reagents	Source	Identifier
Antibodies		
Human RPA	Santa Cruz Biotechnology	sc4842
Human MDC1	Abcam	ab11171
Human RAD50	GeneTex	GTX70228
Human THRAP3	Novus Biologicals	NB100-40848
Human RAD51	Merk Millipore	PC130
Human BRCA	Santa Cruz Biotechnology	sc6954
Human 53BP1	Novus Biologicals	NB100-304
Human XRCC6	ThermoFisher Scientific	MA1-21818
Human γH2AX	Merk Millipore	05-636
Human H2A	Abcam	ab18255
Biotin mouse	Sigma-Aldrich	SAB4200680
Biotin rabbit	Cell Signaling Technology	D5A7
Mouse IgG	Santa Cruz Biotechnology	sc2025
Rabbit IgG	Santa Cruz Biotechnology	sc2027
Mouse IgG-488	Abcam	ab150113
Rabbit IgG-594	Abcam	ab150116
Chemicals, peptides and recombinant proteins		
Cy5-azide	Jena Bioscience	CLK-047
Micrococcal nuclease	New England Biolabs	MO247S
Terminal Deoxynucleotidyl Transferase	ThermoFischer Scientific	EP0162
Biotin-11-dCTP	Jena Bioscience	NU-809-BIOX-L
Streptavidin Magnetic Beads	New England BioLabs	S1420S
Dynabeads ProteinG	Invitrogen	10004D
Sera-Mag-Magnetic Carboxylate A	GE Healthcare	GE24152105050250
Sera-Mag-Magnetic Carboxylate B	GE Healthcare	GE44152105050250
G9A inhibitor	Sigma-Aldrich	B9311
Etoposide	VWR International	CAYM12092
Olaparib	Hölzel Diagnostika	TMO-T3015
Hydroxyl-Tamoxifen	Sigma-Aldrich	H6278
Auxin, Indole-3-acetic acid sodium salt	Sigma-Aldrich	I5148
$^{12}C_6{}^{14}N_4$ l-arginine	Silantes	201003902
$^{12}C_6{}^{14}N_2$ l-lysine	Silantes	211003902
$^{13}C_6{}^{14}N_4$ l-arginine	Silantes	201203902
$^{12}C_6{}^{14}N_2\text{-}d_4$ l-lysine	Silantes	211103913
$^{13}C_6{}^{15}N_4$ l-arginine	Silantes	201603902
$^{13}C_6{}^{15}N_2$ l-lysine	Silantes	211603902
Oligonucleotides		
ON-TARGETplus siRNA 53BP1	Dharmacon	L-003548-00
ON-TARGETplus siRNA ADNP	Dharmacon	L-012857-01
ON-TARGETplus siRNA ATAD2	Dharmacon	L-017603-00
ON-TARGETplus siRNA BRG1	Dharmacon	L-010431-00
ON-TARGETplus siRNA HMGA2	Dharmacon	L-013495-00
ON-TARGETplus Non-targeting siRNA	Dharmacon	D-001810-01
ON-TARGETplus siRNA NuMA	Dharmacon	L-005272-00
ON-TARGETplus siRNA PHF14	Dharmacon	L-020678-01
ON-TARGETplus siRNA PRPF8	Dharmacon	L-012252-00
ON-TARGETplus siRNA RAD51	Dharmacon	L-003530-00
ON-TARGETplus siRNA RPA	Dharmacon	L-015749-01
ON-TARGETplus siRNA SMARCA1	Dharmacon	L-011392-00
ON-TARGETplus siRNA SMARCE1	Dharmacon	L-017522-00
ON-TARGETplus siRNA THRAP3	Dharmacon	L-019907-00
ON-TARGETplus siRNA TPX2	Dharmacon	L-010571-00
ON-TARGETplus siRNA TRA2b	Dharmacon	L-007278-00
Recombinant DNA		
Plasmid: pRRL SFFV d20GFP.T2A.mTagBFP Donor	Addgene	#31485
Plasmid: pRRL sEF1a HA.NLS.Sce(opt).T2A.IFP	Addgene	#31484

5 Gy ionizing radiation (heavy) elicited with Gammacell 40 Exactor (Best Theratronics). Control sample labeled in light corresponds to a 1:1 mix of 12×10^6 untreated cells and 12×10^6 irradiated cells as above. Cell pellets were resuspended in 5 ml of lysis buffer 1 (50 mM HEPES-KOH pH 7.5, 140 mM NaCl, 1 mM EDTA, 10% glycerol, 0.5% NP-40, 0.25% Triton X-100), rotated on the wheel at 4°C for 10 min and spun at 400 *g* for 5 min at 4°C. Pellets were then resuspended in 5 ml of lysis buffer 2 (10 mM Tris-HCl pH 7.5, 200 mM NaCl, 1 mM EDTA), rotated for 10 min on the wheel at RT and spun at 400 *g* for 5 min at RT. Pellets were resuspended in 1.8 ml of lysis buffer 3 (10 mM Tris-HCl pH 7.5, 100 mM NaCl, 1 mM EDTA) and split in 6×1.5 ml sonication tubes (Diagenode). Upon 8 cycles of sonication with Pico Bioruptor (Diagenode) (30 s ON/ 30 s OFF), Triton X-100 (1% final concentration) was added to the samples and the tubes were spun at 400 *g*. Supernatants from the same SILAC labeling were pooled. The su-

pernatant from medium and heavy samples were combined in equal amounts and subjected to ChIP against target protein (between 5 and 15 μg of antibody depending on the target), light-labeled controls were subjected to ChIP with isogenic IgG and used as internal control. After overnight incubation in the cold room, ProteinG magnetic beads previously coated overnight with BSA 0.5% in PBS1× (100 μl per 10 μg of antibody) were added. After 3 h of rotating in the cold room, the beads were cleaned up with Tris–HCl 10 mM. Next, the beads were treated with terminal deoxynucleotidyl transferase (EP0162) and biotinylated nucleotides (Biotin-11-dCTP, Jena Bioscience). The beads were then washed with IP buffer (50 mM Tris–HCl pH 7.5, 1% Triton X-100, 0.5% NP-40, 5 mM EDTA), and proteins were eluted with elution buffer (7.5% SDS, 200 mM DTT) for 15 min at 37°C. Eluted samples were diluted in IP buffer and combined. Then, 100 μl of protease-resistant streptavidin (or prS (26)) beads were added for the DNA enrichment. To analyze the soluble interactors, supernatant was concentrated with speedvac, subjected to SP3 protein clean up as previously described (30,31) and eluted in Am-Bic 50 mM prior digestion with 300 ng trypsin (Promega V5280). For the on-chromatin interactors, prS beads were washed three times with SDS washing buffer (10 mM Tris–HCl pH 8, 1% SDS, 200 mM NaCl, 1 mM EDTA), once with BW2x buffer (10 mM Tris–HCl pH 8, 0.1% Triton X-100, 2 M NaCl, 1 mM EDTA), once with isopropanol 20% in water, and three times with acetonitrile 40% in water. The beads were transferred to PCR tubes using acetonitrile 40%. The supernatant was removed, and the beads were resuspended in 15 μl of 50 mM AmBic-10 mM DTT. Then, the samples were incubated at 50°C for 15 min to reduce the disulfide bonds. The cysteines were alkylated with 20 mM iodoacetamide (IAA) final concentration for 15 min in the dark. IAA was neutralized by adding 10 mM dithiothreitol (DTT) final concentration. To digest the proteins, 300 ng of trypsin (Promega V5280) was added to each tube. The digestion was performed for 18 h and peptides were cleaned using SP3 beads and eluted in 0.1% trifluoroacetic acid (TFA) before mass spectrometry analysis.

For the experimental design shown in Figure 3, light-, medium- and heavy-labeled cells were collected at untreated conditions or after 30 min, 1, 4, 8 h upon 5 Gy IR. At each time-point, light-labeled sample was used for ChIP with isogenic IgG, while medium- and heavy-labeled samples were subjected to H2A and γH2AX ChIP (10 μg of antibody). Samples were then mixed in equal amounts before DNA labeling. The rest of the procedure was carried out as described above.

Isolation of protein on chromatin (or iPOC) during double-strand break repair

Per each experiment, 40×10^6 U2OS cells were metabolically labeled in SILAC (29) DMEM medium containing light (Arg0, Lys0), medium (Arg6, Lys4) or heavy (Arg10, Lys8) amino acids. Medium- and heavy-labeled samples were also treated with 5-ethynyl-2'-deoxyuridine (or EdU) for 18 h at a final concentration of 20 μM. Light- and medium-labeled samples were collected in untreated conditions, while heavy labeled cells were harvested at 1, 4 or

8 h upon 5 Gy ionizing radiations. Each cell pellet was crosslinked with methanol-free formaldehyde at 1% final concentration for 10 min; the reaction was then quenched with glycine 130 mM final for 5 min. Cell pellets were washed twice in PBS 1× and resuspended in 4 ml of permeabilization buffer (0.25% Triton X-100 in PBS1×), incubated for 30 min at RT and spun at 4°C for 5 min at 900 *g*. Pellets were washed once with cold 0.5% BSA in PBS 1× and once with PBS 1×. Upon centrifugation as above, each pellet was resuspended in 5 ml of click reaction mix (10 μM biotin azide, Jena Bioscience CLK-047), 10 mM sodium ascorbate, 2 mM CuSO4 in PBS 1×) and rotated on the wheel, at RT, in the dark for 3 h. Samples were then spun and washed once with 0.5% BSA in PBS1× and once with PBS 1× as above. The pellet was resuspended in 400 μl of lysis buffer (1% SDS, 50 mM Tris-HCl pH 7.5) and sonicated with the Pico Bioruptor (Diagenode) for 20 cycles (30 s ON/ 30 s OFF) or until a chromatin input focused around 600–700 bp. Differently labeled samples were then spun at RT for 10 min at 16 000 *g*, and supernatants were combined in equal amount before adding 200 μl of magnetic prS beads (26) pre-conditioned with lysis buffer. Samples were rotated overnight on the wheel. Supernatant was discarded and prS beads-chromatin sample complexes were recovered on the magnet, washed once with lysis buffer and once with 1 M NaCl. PrS beads-chromatin sample complexes where conditioned in AmBic 50 mM, then resuspended in 30 μl of 50 mM AmBic-10 mM DTT. Then, the samples were incubated at 50°C for 15 min to reduce disulfide bonds, followed by cysteines alkylation with 20 mM IAA for 15 min in the dark. IAA was neutralized by adding 10 mM DTT final concentration and proteins were digested with 300 ng of trypsin (Promega V5280) for 18 h. Peptides were cleaned using SP3 protocol as previously described (30,31), and peptides were then eluted in 0.1% trifluoroacetic acid (TFA). Ammonium formate 20 mM final concentration was added to each sample before subjecting them to fractionation using high-pH reverse-phase chromatography. Peptides were fractionated on an Agilent 1200 Infinity HPLC system with a Gemini C18 column (3 μm, 110 Å, 100 × 1.0 mm, Phenomenex) using a linear 60 min gradient from 0% to 35% (v/v) acetonitrile in 20 mM ammonium formate (pH 10) at a flow rate of 0.1 ml/min. Elution of peptides was detected with a variable-wavelength UV detector set to 254 nm. Thirty-two 1-min fractions were collected and subsequently pooled into four fractions per sample.

Chromatin preparation and fractionation to study the global dynamics of determinants during DNA repair

U2OS cells were metabolically labeled in SILAC (29) DMEM medium containing light (Arg0, Lys0), medium (Arg6, Lys4) or heavy (Arg10, Lys8) amino acids. Each cell pellet corresponded to 24×10^6 cells cross-linked with formaldehyde 1% final concentration. Medium-labeled samples were collected after either 30 min or 4 h from DSB induction with 5 Gy ionizing radiations (IR) with Gammacell 40 Exactor (Best Theratronics), while heavy-labeled cells were harvested after either 1 or 8 h from IR. Cells labeled with light amino acids were collected in untreated conditions and used as a common reference channel be-

tween the two triple SILAC experiments. The first SILAC experiment contained cells untreated, 30 min and 1 h upon IR, labeled in light, medium and heavy channel, respectively. In the second experiment cells untreated, 4 and 8 h upon IR were labeled in light, medium and heavy, respectively. Cell pellets from the same experiment were resuspended in lysis buffer 1 (50 mM HEPES-KOH pH 7.5, 140 mM NaCl, 1 mM EDTA, 10% glycerol, 0.5% NP-40, 0.25% Triton X-100) and mixed in equal amounts into the two triple SILAC experiments. Cells were then rotated on the wheel at 4°C for 10 min and spun at 400 *g* for 5 min at 4°C, ultimately resuspended in lysis buffer 2 (10 mM Tris-HCl pH 7.5, 200 mM NaCl, 1 mM EDTA). Upon rotation for 10 min on the wheel at RT and centrifugation at 400 *g* for 5 min at RT, the pellets were resuspended in lysis buffer 3 (10 mM Tris-HCl pH 7.5, 100 mM NaCl, 1 mM EDTA) and subjected to 8 cycles of sonication with Pico Bioruptor (Diagenode) (30 s ON/ 30 s OFF). Triton X-100 1% final concentration was added to the samples and the tubes were spun at 400 *g*. Per each experiment, 20 μg of chromatin was subjected to buffer exchange through SP3 protein clean up protocol (30) and resuspended in AmBic-10 mM DTT before proteins digestion with 1:50 trypsin (Promega V5280) for 18 h. Peptides were cleaned using SP3 beads and eluted in 0.1% trifluoroacetic acid (TFA) plus 20 mM ammonium formate pH 10 final concentration before high pH reverse-phase chromatography fractionation. Peptides were fractionated on an Agilent 1200 Infinity HPLC system with a Gemini C18 column (3 μm, 110 Å, 100 × 1.0 mm, Phenomenex) using a linear 60 min gradient from 0% to 35% (v/v) acetonitrile in 20 mM ammonium formate (pH 10) at a flow rate of 0.1 ml/min. Elution of peptides was detected with a variable wavelength UV detector set to 254 nm. Forty 1-min fractions were collected and subsequently pooled into 8 fractions per sample experiment.

Profiling of histone post-translational modifications during DNA repair in native conditions and at mononucleosome resolution

Native Chromatin Proteomic (or N-ChroP) protocol was performed as described before (27,28) with some modifications. Fifty million U2OS cells were collected in untreated conditions or 30 min, 1, 4, 8 h recovery from 5 Gy ionizing radiations elicited with Gammacell 40 Exactor (Best Theratronics) and resuspended in Native lysis buffer (10% sucrose, 0.5 mM EGTA pH 8.0, 15 mM NaCl, 60 mM KCl, 15 mM HEPES, 0.5% Triton, 0.5 mM PMSF, 1 mM DTT, 5 mM NAF, 5 mM Na_3VO_4, 5 mM NaButyrate), supplemented with Triton X-100 0.5% final concentration and incubated for 10min on the wheel at 4°C. Nuclei were isolated via centrifugation on a sucrose cushion (Native lysis buffer with 20% sucrose) at 2800 *g* for 30 min, at 4°C. Pelleted nuclei were washed twice with PBS 1× at RT and resuspended in MNase digestion buffer (0.32 M sucrose, 50 mM Tris-HCl pH 7.5, 4 mM $MgCl_2$, 1 mM $CaCl_2$, 0.1 mM PMSF) digested to mononucleosomes with 0.01 U/μl micrococcal nuclease (New England Biolabs, MO247S) at 37°C and spun at 2800 *g* for 10 min at 4°C. After saving 30 μg as input, the supernatant was used for ChIP with γH2AX overnight, at 4°C on the wheel. ProteinG magnetic beads,

pre-conditioned with BSA 0.5% in PBS1× (100 μL per 10 μg of antibody), were then added and left rotating for 3 h at 4°C. Beads were then recovered on the magnet and washed twice with native washing buffer A (or WBA: 50 mM Tris-HCl pH 7.5, 75 mM NaCl, 10 mM EDTA), once with native washing buffer B (WBA with 125 mM NaCl) and once with native washing buffer C (WBA with 175 mM NaCl). Immunopurified material and respective input were separated by SDS-PAGE. After Coomassie staining, histone bands were excised from the gel, and de-stained with six washes of alternate 0, 50%, 100% acetonitrile. Histones were then chemically alkylated with D6-acetic anhydride (Sigma 175641) in 1 M AmBic for 3 h at 37°C, followed by acetonitrile washes as above and in-gel tryptic digestion. Peptides were extracted from the gel with 3 × 100% acetonitrile, 1 × 5% formic acid, 2 × 100% acetonitrile washes. Supernatants containing peptides were pooled, concentrated with speedvac and desalted with self-made StageTips (32) with C_{18} resin. Eluted peptides were lyophilized, resuspended in 0.1% TFA and analyzed with Q-Exactive HF (Thermo Scientific) mass spectrometer. Acquisition details under 'Mass spectrometry data acquisition'.

Mass spectrometry data acquisition

Peptides were loaded on a trap column (PepMap100 C18 Nano-Trap 100 μm × 20 mm) and separated over a 25 cm analytical column (Waters nanoEase BEH, 75 μm × 250 mm, C18, 1.7 μm, 130 Å) using the Thermo Easy nLC 1200 nanospray source (Thermo Easy nLC 1200, Thermo Fisher Scientific). Solvent A was water with 0.1% formic acid and solvent B was 80% acetonitrile, 0.1% formic acid. During the elution step, the percentage of solvent B increased in a linear fashion from 3 to 8% in 4 min, then increased to 10% in 2 min, to 32% in 68 min, to 50% in 12 min and finally to 100% in a further 1 min and went down to 3% for the last 11 min. Peptides were analyzed on a Tri-Hybrid Orbitrap Fusion mass spectrometer (Thermo Fisher Scientific) operated in positive (+2.5 kV) data dependent acquisition mode with HCD fragmentation. The MS1 and MS2 scans were acquired in the Orbitrap and ion trap, respectively, with a total cycle time of 3 s. MS1 detection occurred at 120 000 resolution, AGC target 1E6, maximal injection time 50 ms and a scan range of 375–1500 *m/z*. Peptides with charge states 2–4 were selected for fragmentation with an exclusion duration of 40 s. MS2 occurred with NCE 33%, detection in topN mode and scan rate was set to Rapid. AGC target was 1E4 and maximal injection time allowed of 50 ms. Data were recorded in centroid mode.

For histone samples, peptides were loaded and separated on same trap and analytical columns as above, but the percentage of solvent B increased in a linear fashion from 8 to 40% in 100 min, then increased to 60% in 3 min, to 95% in 5 min and remained 95% for 3 min before going back to 8% for 5 min. Peptides were analyzed on a Q-Exactive HF Orbitrap mass spectrometer (ThermoFisher Scientific) operated in positive (+2.5 kV) data dependent acquisition mode with HCD fragmentation. MS1 detection occurred at 60 000 resolution, AGC target 3E6 maximal injection time 150 ms and a scan range of 300–1500 *m/z*. Peptides with

charge states 2–5 were selected for fragmentation with an exclusion duration of 60 s. MS2 occurred with NCE 30%, detection in top20 mode. AGC target was 5E4 and maximal injection time allowed of 250 ms. Data were recorded in centroid mode.

MS data processing, analysis and data visualization

Mass spectrometry data were processed with MaxQuant software (1.5.2.8, 1.6.2.6) (33,34) using default settings. MSMS spectra were searched against the Human UniProt database concatenated to a database containing protein sequences of contaminants. Enzyme specificity was set to trypsin/P, allowing a maximum of two missed cleavages. Cysteine carbamidomethylation was set as fixed modification, while methionine oxidation and protein N-terminal acetylation were used as variable modifications. Global false discovery rate for both protein and peptides was set to 1%. The match-between-runs and re-quantify options were enabled. Intensity-based quantification options (iBAQ and LFQ) were calculated. Perseus software was used for data visualization (34); after canonical filtering (reverse, potential contaminants and proteins only identified by site), only proteins with at least 1 unique peptide in all the replicates were considered as identified while only proteins with LFQ or SILAC ratio in all the replicates were defined as quantified. Pathway enrichment analysis was performed using the Metascape web software (35).

Survival probability plot was generated with UCSC Xena (http://xena.ucsc.edu), while log2 RNA seq data visualization was performed with firebrowse (http://firebrowse.org). Boxplots were generated with R studio, R (https://rstudio.com) or boxplotr web software (http://shiny.chemgrid.org/boxplotr/). STRING web software (https://string-db.org/) was adopted for functional protein association network visualization.

Immunofluorescence in AID-DIvA cells

For immunofluorescence, around 1×10^4 AID-DIvA cells (36) were seeded in 24-well plates on glass coverslips in DMEM medium without antibiotics for 10 h. Cells were then transfected with 10 nM final concentration of control or target siRNAs using Lipofectamine™ RNAiMAX (ThermoFisher Scientific), according to the manufacturer's instructions, medium was then replaced with complete medium after 8 h. Seventy-two hours post-transfection, DSBs were induced with 300 nM hydroxyl tamoxifen (4-OHT Sigma-Aldrich H6278) for 4 h. Repair was promoted via adding 500 μg/ml auxin (indole-3-acetic acid sodium salt, Sigma-Aldrich I5148) for 1 h, triggering degradation of the AsiSI enzyme. Cells were fixed with 4% formaldehyde for 10 min and permeabilized with 0.2% Triton X-100 for 10 min while on shaking. For Supplementary Figure S5A,B, cells were subjected to a click-chemistry reaction with 20 mM of Cy5- or Biotin-azide (Jena Bioscience) for 30 min. Biotin-azide samples were incubated afterward with DNA hydrolysis buffer (1.5 M HCl) for 30 min, followed by three washes with PBS 1×. For Figure 3D, U2OS cells were used in immunofluorescence and DSB were induced with 5 Gy ionizing radiations with a Gammacell 40

Exactor (Best Theratronics), and cells were fixed and permeabilized 1 h upon IR. All cells were incubated with blocking solution (1% BSA, 22.52 mg/ml glycine in PBS-Tween 20, 0.1%) for 1 h while shaking. Immunostaining was performed overnight in a humidified chamber with antibody diluted in blocking solution. Antibodies against γH2AX (Millipore, 05–636), THRAP3 (Novus Biologicals, NB100-40848) were used at 1:1000 dilution, and antibody anti-RAD51 (Millipore, PC-130) and anti-BRCA1 (Santa Cruz Biotechnology, sc6954) were incubated at 1:100 and 1:50, respectively. After washes, secondary antibodies were added at 1:500 dilution for 1 h, followed by washes with PBS1×. In the second wash, Hoechst at 1:1000 was added. Upon coverslip mounting, images were acquired with a Zeiss Cell Observer inverted microscope (Zeiss) with an oil objective at 63× magnification. Images were analyzed with ImageJ software (imagej.nih.gov/ij), where Hoechst or DAPI was used to count the number of cells and define nuclei boundaries as ROIs. RAD51-, BRCA- and γH2AX-foci were counted within each nucleus with an in-house developed Java Macro after background subtraction with rolling ball radius of 50 pixels. Minimum size restrictions were adopted and only foci with at least 0.2 and 0.15 micron^2 were counted for RAD51, BRCA and γH2AX, respectively. In all conditions, at least 50 cells were imaged and the number of foci was represented as boxplot in comparison with non-targeting silencing control. Significance was calculated with One-way ANOVA statistics and *, ** and *** correspond to P-values lower than 0.05, 0.001 and 0.0001, respectively. For co-localization between γH2AX and THRAP3 in Figure 3D upper panel, the 'Colocalization threshold' ImageJ plug-in was used, adopting default settings.

Proximity ligation assay

Proximity ligation assay (PLA) was performed with Duolink® Proximity Ligation Assay (Sigma-Aldrich-Merck, DUO92102) according to manufacturer's instructions. In brief, 1×10^4 U2OS cells were seeded on glass coverslip and after 12 h were either left untreated, or DSBs were induced with 5 Gy ionizing radiation with a Gammacell 40 Exactor (Best Theratronics). Cells were then fixed, permeabilized as in the immunofluorescence protocol above. Blocking and incubation with primary antibodies against γH2AX (Millipore, 05–636) and THRAP3 (Novus Biologicals, NB100-40848) were performed overnight in a humidified chamber. PLA mouse and rabbit probes were added and ligated, before rolling circle amplification according to the manufacturer's instructions. Slide preparation and imaging acquisition were performed as in the immufluorescence protocol above. DAPI staining was used to count nuclei and for defining nuclei boundaries as ROIs. PLA products per nucleus were counted with ImageJ using in-house developed Java Macro after background subtraction with rolling ball radius of 10 pixels. The number of colocalization events is reported in boxplot for untreated and IR conditions. Significance was calculated with one-way ANOVA statistics, and *** corresponds to a P-value lower than 0.0001.

Cell cycle analysis by flow cytometry

Flow cytometric analysis was performed as previously described (37). Briefly, cells were transfected with 10 nM final concentration of control or target siRNAs using Lipofectamine™ RNAiMAX (Thermo Fisher Scientific), according to the manufacturer's instructions. After 72 h cells were fixed overnight with ice-cold 70% ethanol, and then permeabilized in phosphate buffer solution (PBS) containing 0.25% Triton X-100 (Sigma). DNA was stained with 50 μg/ml propidium iodide (PI, Sigma-Aldrich) in PBS containing 0.1% Triton-X-100 and 200 μg/ml DNase free RNase A (Sigma-Aldrich). Measurements were performed on a BD LSRFortessa flow cytometer (BD Biosciences) with FACSDiva software version 8.0.1 (BD Biosciences). 100.000 PI + events were recorded for each condition from three independent experiments. Data analysis was performed using FlowJo X 10.0.7 software (FlowJo).

Traffic light reporter (TLR) assay

Traffic light reporter (TLR) assay was performed as previously described (38,39). In brief, U2OS-TLR cells were transfected with 10nM final concentration of control or target siRNAs using Lipofectamine™ RNAiMAX (Thermo Fisher Scientific), according to the manufacturer's instructions. After 10 h, cells were co-transfected with plasmids expressing I-SceI nuclease fused to infrared fluorescent protein (IFP) and donor plasmid expressing GFP donor sequence fused to blue fluorescent protein (BFP), using Polyjet™ *in vitro* transfection reagent (SignaGen Laboratories) according to the manufacturer's instructions. Seventy-two hours after siRNA transfection, cells were harvested, and GFP and mCherry signals (reflecting HDR and NHEJ, respectively) were measured by four-color fluorescent flow-cytometry using a BD LSRFortessa flow cytometer (BD Biosciences). A minimum of 10.000 double-positive (IFP+/ BFP+) cells were recorded for each condition from three independent experiments. Data analysis was performed using FlowJo X 10.0.7 software (FlowJo). Results of siRNA-transfected cells were normalized to control siRNA-transfected cells. U2OS ID3-GFP (kindly provided by Dr Ali Bakr, DKFZ) and U2OS m53BP1-mCherry cells (40) (kindly provided by Prof. Randi Syljuåsen, Oslo University Hospital) were used for compensation in flow cytometry.

Colony formation assay, PARP inhibition and etoposide treatment

Colonigenic assays were performed as previously described (41) with some modifications. In brief, U2OS cells were plated overnight in complete medium without antibiotics at 20–25% density. Cells were then subjected to siRNA transfection with 10 nM final concentration of control or target siRNAs using Lipofectamine™ RNAiMAX (Thermo Fisher Scientific), according to manufacturer's instructions. After 24 h post transfection, cells were collected, counted and seeded in a 6-well plate at a density of 1000 cells per well. Forty-eight hours post transfection, cells were incubated for 2 h with 1 μM PARP inhibitor or solvent control, followed by DSB induction via 1 μM etoposide treatment for 2 h or solvent control. For Figure 2E, cells were treated for 24 h with etoposide at 0.1, 0.5, 1 or 10 μM. For G9A colony formation assay, cells were exposed for 4 h to 5 μM G9Ai before incubation with PARPi. After 10–14 days, colonies were fixed for 10 min in 70% ethanol, stained with crystal violet, destained in water and visualized. Colonies were counted with ImageJ software (imagej.nih.gov/ij) with an in-house developed Java Macro upon setting the image threshold and defining well boundary as ROI. Number of colonies or surface area (normalized on reference) was normalized on non-targeting silencing control. Values from three biological replicates were averaged and displayed as mean ± standard deviation.

Quantification and statistical analysis

SigmaPlot software was used to create graphs, perform statistical tests and calculate *P*-values among at least three biological replicates. Unless stated otherwise, one-way ANOVA statistics was used for multiple comparison analysis. Each figure legend and respective method sections indicate both statistical significance and reference used for calculation of the *P*-value. For DDR-induced protein modulation, targets were classified as recruited or evicted if they fall in ± 5%, respectively, of the 90 percentile log2 ratio distribution. Ratios of identified proteins with an intensity value (LFQ or iBAQ) only in either DDR-treated or untreated SILAC channels were replaced by a fixed value corresponding to ± 6.67 in log2, respectively. Volcano plots were generated with Perseus software via a two-side *t*-test statistics, FDR > 0.05, S0 equal to 0.1. When reported, z-score normalization was performed per experiment (or column *z*-score normalization) with Perseus software. For the analysis of hPTM, the extracted ion chromatography (or XIC) was used as a measure of abundance of each modification. The relative abundance (or RA) is calculated as the XIC of a modified peak over the sum of all the XICs of all peaks for the same peptide multiplied by 100. In the heatmap RA over untreated time points are reported. The relative enrichment of a particular modification is calculated as the ratio of its RA in the ChIP over its RA in the chromatin input. Histone modifications with a log2 ratio higher or lower than 1 were considered as enriched or depleted, respectively.

Data and code availability

The webpage-based viewer for the experiments described in this manuscript is available at 'https://chromatin-proteomics.dkfz.de/'.

The mass spectrometry proteomics data have been deposited to the ProteomeXchange Consortium via the PRIDE (https://www.ebi.ac. uk/pride/) (42) partner repository with the dataset identifier PXD027421.

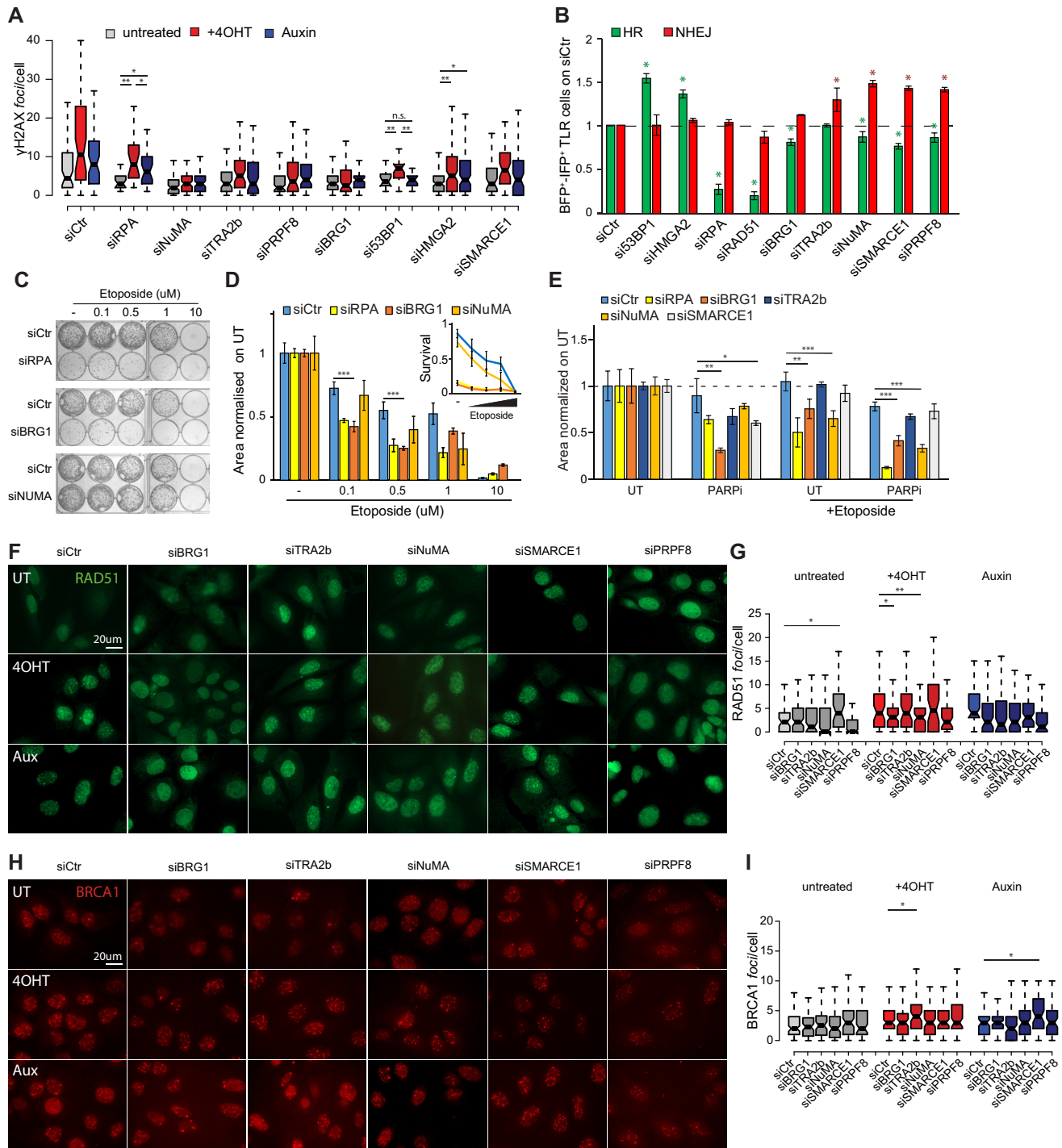The ChIP-SICAP protocol is maintained at protocols.io: dx.doi.org/ 10.17504/protocols.io.bcrriv56.

Figure 2. Functional characterization of RPA- and MDC1-specific on-chromatin interactors. (**A**) Number of γH2AX *foci* per nucleus in AID-DIvA cells left untreated, upon DSB induction, and during DSBs repair (untreated, +4OHT and Auxin, respectively) upon knockdown for targets interacting with either RPA or MDC1 in comparison with on-target non-targeting silencing control (siCtr). (**B**) Quantification of homologous recombination (green) and NHEJ (red) repair events in traffic-light reporter (U2OS-TLR) cells depleted of protein candidates and normalized on silencing control (siCtr). Green and red asterisks reflect significant regulation in HR and NHEJ, respectively, in respect to siCtr (ANOVA-based statistics). Mean values of at least three biological replicates with standard deviation are shown. (**C**) Colony formation assay at increasing amounts of etoposide in cells knockdown for proteins important for HR repair (BRG1) or pathway choice (NuMA) compared with silencing control (siCtr). Silencing of RPA (siRPA) is used as internal control. (**D**) Quantification of (C), mean values normalized on untreated condition (UT) and standard deviations are reported. Zoom-in shows the survival of cells upon target knockdown compared with silencing control. Mean values of at least three biological replicates with standard deviation are shown. (**E**) Quantification of colony formation assay in U2OS cells depleted of listed proteins involved in either HR or pathway choice and subjected to PARP (PARPi) alone or in combination with etoposide to promote DSBs formation. Mean values from three biological replicates normalized on untreated condition (UT) are shown, error bars represent standard deviations. Representative immunofluorescence images of RAD51 (**F**) and BRCA1 (**H**) foci in AID-DIvA cells in untreated (UT) condition, upon DSB formation (4OHT), and during DSB repair (Aux) upon knockdown with indicated targets. siCtr corresponds to on-target non-targeting siRNA. Quantification of RAD51 (**G**) and BRCA1 (**I**) foci in AID-DIvA cells knockdown for targets involved in either HR or pathway choice. *, ** and *** correspond to *P*-value < 0.05, 0.01 and 0.001 of ANOVA statistical test, respectively. n.s. = not statistically significant.

RESULTS

The analysis of DSB-mediated interactome dynamics identifies ON-chromatin binders of MDC1 and RPA upon DSB repair

In this study, we applied complementary proteomic approaches to investigate chromatin composition and dynamics during DSB repair, at the level of global chromatin, protein interactions and hPTMs. First, we employed ChIP-SICAP (25) in cells subjected to ionizing radiation (IR), an efficient inducer of double-strand breaks (DSBs), to identify novel chromatin-bound proteins that are involved in DSB repair. To this end, we targeted five core components of the DNA repair machinery as bait proteins: the tumor suppressor TP53, the MRN complex subunit RAD50, the HR-associated protein RPA, the mediator of checkpoint MDC1, and 53BP1, important for NHEJ. We used a triple-SILAC labeling approach (43) to distinguish specific binders of target proteins from background in IgG controls, and to accurately quantify DSB-induced changes in the interactomes (Figure 1A, Table 1). We classified the interactors into either constitutively associated with the bait (constitutive) or exclusively associated while the bait is in its ON- or OFF-chromatin state. Each bait exhibited a different relative proportion of interactors in the three classes; moreover, by performing such analysis in both untreated and cells subjected to IR, we were able to trace the DSB-mediated interactome dynamics. Our data show that, upon DSBs formation, proteins interacting with RPA, MDC1 and 53BP1 have a more dynamic behavior with 5–10% of the interactors changing their association with the bait (i.e. transition) upon IR; on the contrary, p53 and RAD50 seem to have a more static interactome, with <1% of the binders showing DSB-induced transition (Figure 1B). We then evaluated if common chromatin players were recruited at sites marked by the different DDR proteins, or whether each candidate used as bait in ChIP-SICAP had a rather unique interactome. When collectively looking at interactors associated with the proteins used as bait in their OFF- or ON-chromatin state, intersection of the respective binding proteins revealed that roughly 65% of p53, RAD50 and RPA interactors were identified (65%, 69% and 66%, respectively) when using MDC1 as bait protein. Interestingly, in the same conditions, >80% of proteins associated with the NHEJ target 53BP1 were co-enriched, while additionally identifying 95 unique binders. Similarly, the vast majority of p53 and RAD50 binders (75% and 86%, respectively) were co-purified in RPA ChIP-SICAP experiments (Figure 1C). Since RPA and MDC1 accounted for >90% of the collectively identified interactors, and since RAD50 plays a pivotal role at the junction between NHEJ and HR repair pathways, we further evaluated the IR-induced changes in the ON-chromatin interactomes of these three targets.

In each ChIP-SICAP experiment, the bait was among the most enriched proteins, indicating the specificity of the technique, along with histones, reflecting a successful chromatin enrichment (Supplementary Figure S1A–C). Moreover, in all conditions, between 40 and 75% of the interactors were identified exclusively in the ON-chromatin fraction, thus providing further evidence of the specificity

of the approach (Supplementary Figure S1D–F). Moreover, differently from what we observed before (Figure 1B), when specifically comparing the ON-chromatin interactomes the overlap of shared binders decreased to 20–40% (Figure 1E), thus further suggesting how higher specificity is achieved by focusing on chromatin-mediated functional interactions. Indeed, when using RPA as bait, known components of the HR pathway (e.g. ATR, RPA2 and ETAA1) were strongly recruited on chromatin upon IR, thereby indicating their close proximity to RPA on DNA (Figure 1D). Moreover, specific interactors of RPA belong to gene ontologies (GOs) associated with regulation of DNA damage repair and replication fork processing (Figure 1E,F). In the RAD50 experiment, RPA1 showed strong DDR-induced recruitment, and other proteins that co-enrich with RAD50 are mainly involved in telomere maintenance and p53-mediated signaling (Figure 1D–F). In contrast, ChIP-SICAP for MDC1 identified different core components of the NHEJ machinery (e.g. 53BP1, XRCC5/Ku80 and XRCC6/Ku70), and our results interestingly point toward a specific DNA-mediated interaction among these chromatin proteins (Supplementary Figure S1G–K). Moreover, our data readily revealed also the dynamic ON-chromatin crosstalk between 53BP1 and MDC1, in line with their functional interaction as known readers of γH2AX (Figure 1D, Supplementary Figure S1G). In addition, specific MDC1-interactors enriched GOs terms involved in the DNA repair process (Figure 1D–F). While subunits of the MRN complex were expectedly particularly associated with RAD50, we observed that DNA repair components involved in HR and NHEJ machineries were predominantly enriched in the ON-chromatin fraction of RPA and MDC1, respectively (Figure 1G). As a result, the comparison between pathways associated with either RPA- or MDC1-specific ON-chromatin interactors shows how HR and Fanconi Anemia (FA) are extremely enriched in RPA, while interactors of MDC1 mainly belong to cell cycle and NHEJ (Figure 1H). These results are in line with the notion of MDC1 as a key regulator of the DDR cascade, in contrast with the HR-restricted role of RPA.

Besides known components of the DDR machinery, our analysis identified numerous other proteins interacting with MDC1 or RPA upon IR, but not previously associated with a function in the DDR. Among these, we focused on several candidates to functionally assess their role in DSB repair through either HR or NHEJ repair pathways. From our ChIP-SICAP data, we selected NuMA, TRA2B and PRPF8 as candidates specifically associating with RPA upon DSB formation, and SMARCE1/BAF57 and HMGA2 among the proteins co-enriched with MDC1. Moreover, in light of its strong functional DDR-mediated interaction with both RPA and MDC1, we further investigated the role of SMARCA4/BRG1 (Figure 1I).

ON-chromatin interactors of RPA and MDC1 influence DNA repair by regulating HR, NHEJ or DSB repair pathway choice

To assess the involvement of IR-dependent functional interactors of RPA and MDC1 in DSB repair, we first evaluated whether their silencing had any impact on the forma-

tion and resolution of γH2AX *foci*, an early marker of DSB repair. To this end we took advantage of isogenic U2OS AID-DIvA cells, where the AsiSI enzyme produces a defined number of DSBs upon 4-OHT induction, while DSBs repair is promoted through Auxin-Inducible degradation of the enzyme (36). Upon target knockdown (Supplementary Figure S2A), all tested cells show a substantial decrease in the number of induced γH2AX foci and, besides silencing of the positive control RPA and 53BP1, only depletion of HMGA2 still preserves a statistically significant response to DSBs (Figure 2A). These results therefore suggest that all tested candidates identified *via* ChIP-SICAP are crucial for either γH2AX foci formation or spreading of this marker (e.g. HMGA2) upon IR, implicating their function in DSB repair.

To gain insight into the role of these candidates in DSB repair, we employed isogenic U2OS-traffic-light reporter (U2OS-TLR) cells (39), and used FACS-based quantification to simultaneously evaluate both HR and NHEJ efficiency upon target knockdown. Cells depleted for 53BP1 and RPA/RAD51 were used as positive controls for NHEJ and HR, respectively (Figure 2B). Silencing of HMGA2 results in a strong increase in the number of cells repairing DSBs via HR, while the fraction of NHEJ remains unchanged (Figure 2B and Supplementary Figure S2B,C). In contrast, silencing of BRG1 specifically decreases the efficiency of HR, while inhibition of TRA2B promotes the rate of NHEJ by 20% (Figure 2B and Supplementary Figure S2B,C). These observations clarify the controversial role of HMGA2 in the DDR (44) and indicate how this target binds MDC1 and has a similar function to 53BP1 in negatively regulating HR. In line with previous evidence (45) our results also suggest that BRG1 is recruited at DSBs to promote a chromatin state facilitating HR repair (Figure 2B and Supplementary Figure S2B,C). In addition, besides its canonical function in BRCA1 RNA splicing (46), our results point toward a novel and more direct role for TRA2B in the DDR via inhibition of NHEJ.

In contrast to most site-specific DSB repair systems, the U2OS-TLR assay allows to quantify how individual proteins impact on the equilibrium between NHEJ and HR at induced DSBs. In particular, knockdown of NuMA, SMARCE1 or PRPF8 leads to an increase in NHEJ mirrored by a parallel decrease in HR (Figure 2B and Supplementary Figure S2B,C). These results add functional detail to the suggested involvement of NuMA and PRPF8 in DNA damage repair (47–49), while assigning a completely novel role in the DDR to the BAF/PBAF subunit SMARCE1.

We next selected BRG1 and NuMA as representative proteins important for HR and repair pathway choice, respectively, and evaluated whether their selective involvement in either processes can be effectively distinguished. Knockdown of BRG1, but not NuMA, significantly sensitizes cells to low doses of the DSB-inducer etoposide (from 0.1 to 0.5 μM), to a similar extent as RPA depletion which was used as a positive control for HR impairment (Figure 2C, D). This evidence corroborates the results obtained in the TLR assay (Figure 2B) and indicates how, upon depletion of a pathway choice repair protein (e.g. NuMA), the increased

rate of NHEJ confers partial resistance to low doses of DSB inducer.

Selective impairment in the HR pathway is currently exploited in cancer therapy due to the predisposition to synthetic lethality with PARP inhibitors (PARPi). We therefore challenged our results obtained in the TLR system by exposing cells knockdown for the different targets to Olaparib treatment, either alone or in combination with etoposide. As expected, silencing of HR-related proteins (i.e. BRG1 and RPA) resulted in a pronounced synthetic lethality with PARPi, while knockdown of targets involved in repair pathway choice only partially sensitizes to either Olaparib (i.e. siSMARCE1) or etoposide treatment (i.e. siNuMA) (Figure 2E). These results strongly suggest that, in contrast to HR-deficient cells, the increase in NHEJ observed upon knockdown of a DSB pathway choice regulator might counteract the deficiency in HR, thereby decreasing the sensitivity to PARPi.

To gain further insights in the function of selected target proteins in DSB repair, we monitored the formation of RAD51 and BRCA1 foci, in AID-DIvA cells. Our results revealed that NuMA-depleted cells are defective in RAD51 loading, while siTRA2B cells have a significantly higher number of induced BRCA1 foci, thus providing a potential explanation for their different role in DSBs repair (Figure 2F–I, Supplementary Figure S2F,G). Importantly, none of these results can be explained by a change in cell cycle distribution upon depletion of the target proteins (Supplementary Figure S2D, E).

In summary, we investigated the potential role in DSB repair for candidates associating with either RPA or MDC1 and highlighted that inhibition of each tested candidate has an impact on the DDR as monitored by γH2AX foci formation. Moreover, we assigned a role to these targets in NHEJ (i.e. HMGA2), HR (e.g. BRG1) or the balance between these DSB repair pathways (i.e. NuMA, SMARCE1 and PRPF8). As validation, knockdown of proteins involved in the repair pathway choice increases the rate of NHEJ repair, thereby promoting resistance to PARPi treatment despite the decrease in HR efficiency. Finally, we show that even though NuMA and TRA2B are both enriched at RPA sites in ChIP-SICAP, they exhibit functional differences, thereby suggesting that mediators of the DDR can be recruited at proximal damaged sites but still impinge on DNA repair in distinct ways.

Dynamic profiling of chromatin-associated interactors of γH2AX

γH2AX is the first marker of DSB repair upstream of both NHEJ and HR pathways (50), and MDC1 has been identified as its main reader (51). However, little is known about the identity and dynamics of other chromatin proteins that associate with this fundamental hPTM. To investigate this aspect in a temporally resolved manner, we applied for the first time ChIP-SICAP to an hPTM and used γH2AX as target. We profiled the dynamics of its ON-chromatin interactors in a time course during the DSB repair induced by IR, and employed triple-SILAC labeling to discriminate, at each time point, γH2AX-specific ON-chromatin interactors from general histone (H2A)-associated proteins and
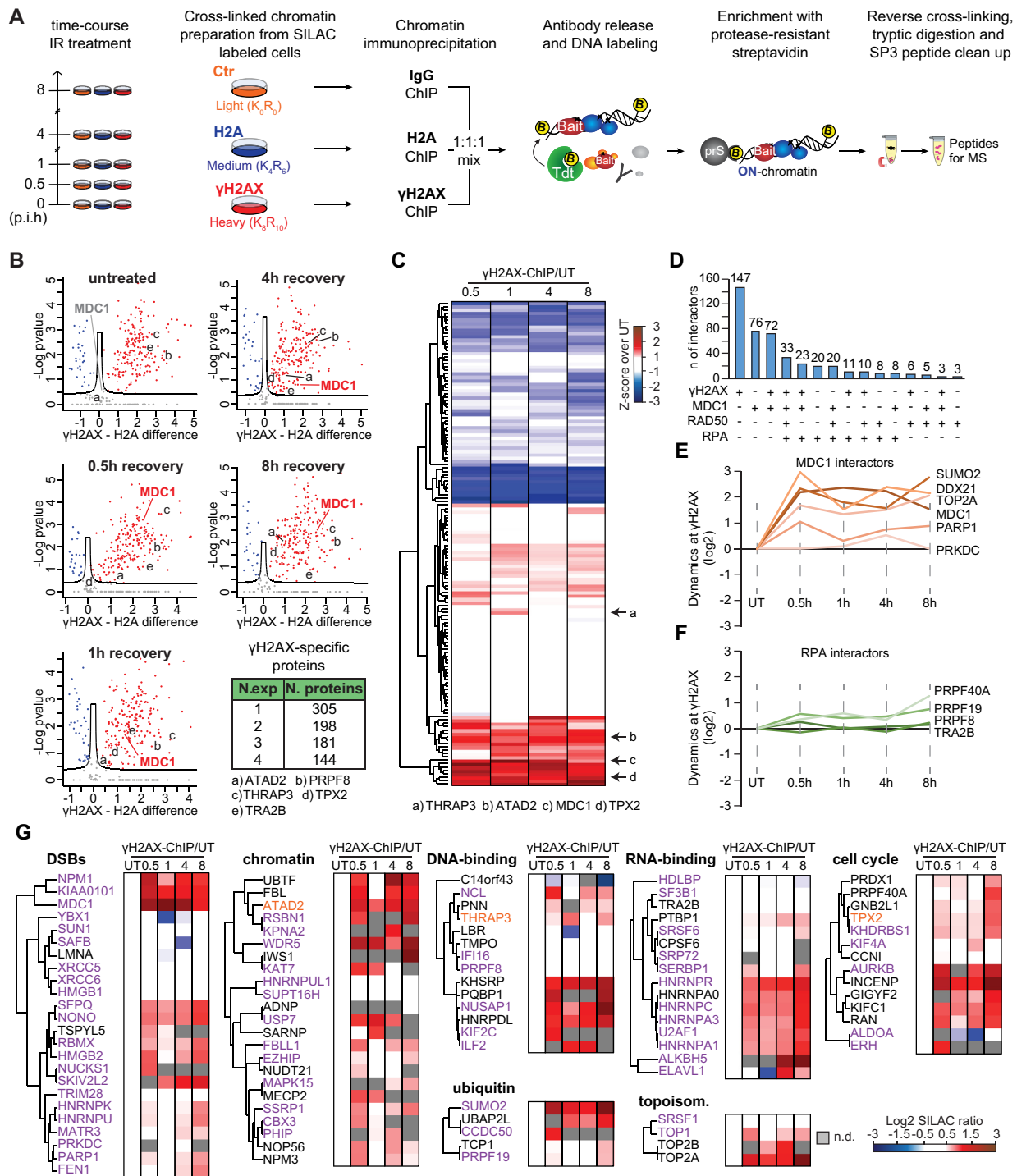
Figure 3. Functional interactors of γH2AX during DNA damage repair. (**A**) Time course ChIP-SICAP experimental design; p.i.h.: hours post-irradiation. At each time point U2OS cells labeled with light-, medium- or heavy-SILAC amino acids were subjected to ChIP-SICAP protocol using IgG control, H2A or γH2AX as bait, respectively. (**B**) Volcano plots represent the fold change difference of *t*-test statistics for γH2AX- and H2A-associated ON-chromatin binders (red and blue, respectively), at different time points during DSBs repair. MDC1 is highlighted as positive control. The table reports the number of γH2AX-specific functional interactors shared among the different experiments during DSBs repair (from untreated condition to 8 h). Panels (A–E) refer to listed γH2AX-specific ON-chromatin functional candidates. (**C**) Heatmap representation of γH2AX-specific ON-chromatin interactors identified at all time points during the DDR. At each time point, log2 ratios over untreated sample are shown upon *z*-score normalization. Red and blue correspond to enriched and evicted γH2AX interactors during DSBs repair, respectively. Panels (A–D) refer to listed ON-chromatin candidates further evaluated. (**D**) Overlay view of number of interactors in common among γH2AX and the DDR-associated proteins used as bait in ChIP-SICAP in Figure 1. Line plots represent the dynamics of MDC1- (**E**), RPA- specific (**F**) ON-chromatin functional interactors at γH2AX-sites during the DDR. (**G**) Heatmap visualization of γH2AX-specific ON-chromatin interactors classified according to their function; SILAC ratio (in log2) between the protein abundance at different time points during the DDR and untreated conditions is shown. Interactors of γH2AX already associated with DSB break repair and novel candidates further evaluated are shown in purple and orange, respectively; n.d. = not determined.

from non-specific background (IgG isotype control) (Figure 3A). Quantitative analysis profiled almost 150 interactors that exclusively associate with γH2AX at all timepoints, this included the strong and IR-dependent enrichment of the γH2AX-reader MDC1, thereby illustrating the efficacy of the time-course ChIP-SICAP approach, also when applied to hPTMs (Figure 3B,C and Supplementary Figure S3A–E).

Among the γH2AX-specific proteins, almost half are linked to regulation of different chromatin-related processes, while the rest have an established role in various other biological processes (Supplementary Figure S3F). In addition, 25 γH2AX-specific interactors have an already established role in DNA repair mechanism (Supplementary Figure S3G). Furthermore, γH2AX-specific interactors enriched at all time-points along the repair process belong to GO associated with SUMO E3 ligases, in line with the well-established role of SUMOylation in DNA repair (52). In the same group, we identified proteins involved in RNA splicing (Supplementary Figure S3H), thus suggesting a possible stabilization of DSB-induced transcripts (53). In contrast, proteins evicted from γH2AX-marked sites were more globally involved in ribosome formation and regulation of translation (Supplementary Figure S3I).

Overlay analysis of ChIP-SICAP data revealed that almost 1/3 of γH2AX interactors are shared with its reader MDC1 (98 proteins), of which 72 are exclusively identified by these two chromatin determinants, while only a minor fraction is exclusively in common with the other DSB-related proteins (Figure 3D and Supplementary Item S1). In addition, our data allow to profile the temporal association between γH2AX and ON-chromatin interactors identified in MDC1, RPA and RAD50 ChIP-SICAP experiments, thus both validating the chromatin association for these binders at damaged sites, and describing their dynamics during the DDR at sites marked by γH2AX (Figure 3E,F and Supplementary Figure S3J). Overall, the majority of the proteins are rapidly recruited at DSB sites, although they follow different kinetics during the DDR. In particular, interactors of MDC1 show the highest dynamics at break sites with a rapid chromatin recruitment, in line with the strong link between γH2AX and its reader (Figure 3E). Most of the RPA and RAD50 binders instead exhibit a lower temporal enrichment at γH2AX-sites, and they are in general recruited more gradually during the repair process (Figure 3F and Supplementary Figure S3J).

Upon clustering γH2AX interactors by biological function and profiling their dynamics during the DDR, our data indicate how proteins with a similar function can follow a different kinetics at break sites, and, conversely how targets belonging to distinct biological processes can associate with γH2AX at the same time during the DDR (Figure 3G). These data provide evidence on the complex and coordinated regulation of chromatin around the break site to ensure an efficient repair process. Beyond the many ON-chromatin interactors of γH2AX with an already reported link with the DDR (purple in Figure 3G), we identified several others that are less thoroughly investigated in this context. This includes the nuclear protein THRAP3, the histone reader ATAD2 and the microtubule organizer TPX2, whose role in the repair process was further investigated in more detail.

In summary, through our time course ChIP-SICAP experiment performed during the DDR and using γH2AX as entry point, we revealed a functionally and temporally diverse set of proteins enriched at chromatin around the break site. These results provide evidence for the intricate and tailored chromatin re-arrangements at DSB sites necessary to ensure an efficient repair process. Among many proteins previously associated with the DDR, this approach also identified and profiled novel candidates whose function in DNA repair remains to be further investigated.

THRAP3 is rapidly recruited to γH2AX sites upon DNA damage

THRAP3 caught our interest because of its recruitment to γH2AX-marked break sites predominantly at 1 h after inducing DSB (Figure 3C and Supplementary Figure S3A–E). THRAP3 was previously reported in an overexpression system to be highly phosphorylated upon DNA repair but to be excluded from micro-irradiated lesions (54). More recently it has been implicated in R-loop resolution through the interaction with DDX5 and XRN2 (55). Our analysis showed that all these three factors associate specifically with γH2AX, albeit at different time points during the DDR (Supplementary Figure S3A–E), suggesting an additional role of THRAP3 beyond R-loop resolution. We therefore first tested the co-localization of endogenous THRAP3 with γH2AX in untreated as well as irradiated cells by means of immunofluorescence (IF) and PLA. Our results verified the interaction between these two chromatin determinants already in untreated conditions and confirmed the significant increase in co-localization between THRAP3 and γH2AX after 1 h recovery upon induction of DSBs (Figure 4A). Furthermore, silencing of THRAP3 impaired γH2AX foci formation but not their repair in AID-DIvA cells system (Figure 4D and Supplementary Figure S4A,C). Moreover, TLR-U2OS cells show a normal balance between NHEJ and HR after knockdown of THRAP3 (Figure 4E and Supplementary Figure S4D,E). Taken together, our results suggest that THRAP3 is specifically but transiently associated with γH2AX. Functionally, it affects both DSB repair pathways leaving the balance between NHEJ and HR untouched. These results, point toward a more structural role and possible involvement of THRAP3 in either promoting the splicing of mRNA encoding for repair proteins important for γH2AX foci formation, or in the stabilization of DNA damage-induced RNAs at DSB sites.

ATAD2 and TPX2 stably interact with γH2AX during DNA damage repair and play a key role in HR

Among the proteins strongly enriched at γH2AX at all time-points during the DDR, we robustly identified the specific γH2AX-reader MDC1, as well as the topoisomerase IIα and the helicase DDX21, two enzymes involved in DNA and R-loop unwinding and regulating genome stability (56,57) (Figure 3E,G and Supplementary Figure S3H). This encouraged us to further investigate proteins with a
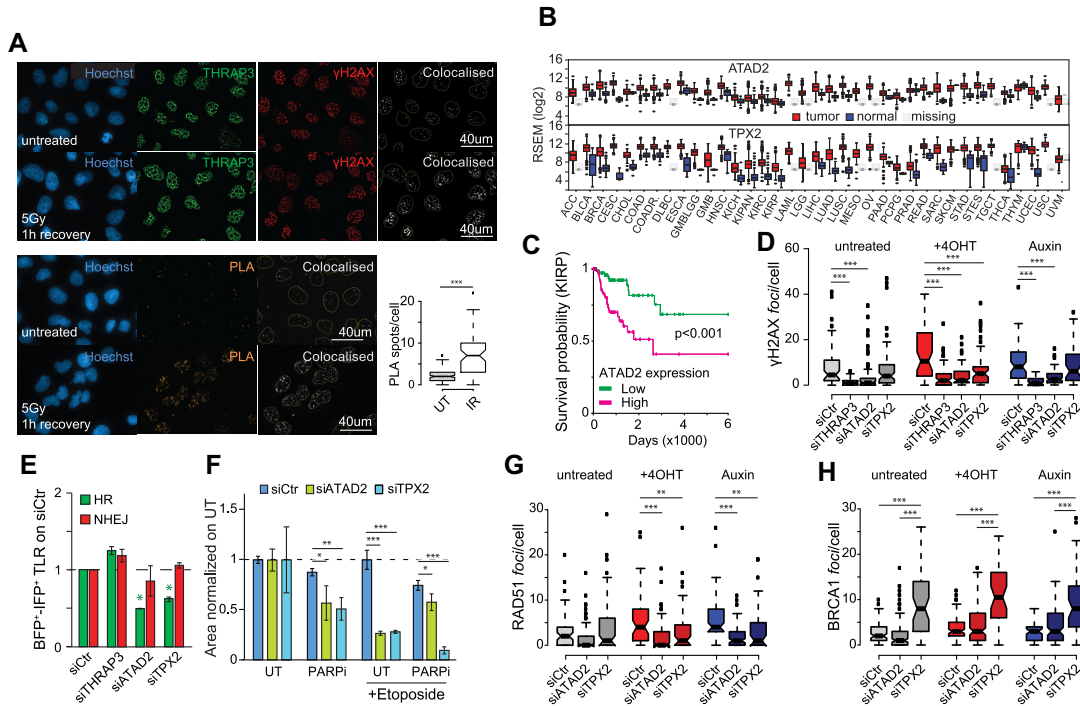
Figure 4. IR elicits functional interaction between THRAP3 and γH2AX, while ATAD2 and TPX2 mediate DSB repair through HR. (**A**) Immunofluorescence (top panel) and proximity ligation assay (PLA, bottom panel) validation of DSB-mediated interaction between THRAP3 and γH2AX. Boxplot shows the quantification of PLA assay in untreated cells (UT) and cells exposed to ionizing radiation (IR, 5 Gy, 1 h recovery). (**B**) Deregulation of ATAD2 (top) or TPX2 (bottom) RNA level in tumor samples (red) compared to normal tissues (blue) from TCGA expressed as log2 RNAseq by Expectation-Maximization (or RSEM). (**C**) Survival probability of patients affected by Kidney renal papillary cell carcinoma (KIRP) with low (green) or high (pink) ATAD2 levels. (**D**) Number of γH2AX foci per nucleus in AID-DIvA cells left untreated or subjected to DSBs induction and repair (tamoxifen/+4OHT and Auxin, respectively), after knockdown for THRAP3, ATAD2 or TPX2 in comparison with on-target non-targeting silencing control (siCtr). Significance over siCtr is shown. (**E**) Quantification of HR (green) and NHEJ (red) repair events in U2OS-TLR cells depleted for THRAP3, ATAD2, or TPX2 and normalized over non-targeting silencing control (siCtr). Green and red asterisks reflect significant regulation in HR and NHEJ, respectively, in respect to siCtr. (**F**) Quantification of CFA in U2OS cells depleted of either ATAD2 (light green) or TPX2 (light blue) and subjected to PARP inhibitor (PARPi) alone or in combination with etoposide to promote DSBs formation. Mean values of three biological replicates normalized on untreated (UT) with standard deviations are shown. Quantification of RAD51 (**G**) and BRCA1 (**H**) foci in AID-DIvA cells knockdown for targets involved in either HR or pathway choice. *, ** and *** correspond to *P*-value < 0.05, 0.01 and 0.001 of ANOVA statistical test, respectively.

similar temporal trend at γH2AX sites, yet with a poorly characterized role in the DDR. In particular, within this cluster of proteins we focused our attention on the spindle protein TPX2 and the transcriptional co-activator ATAD2 (Figure 3B,C,G and Supplementary Figure S3A–E). Upon IR, TPX2 has been reported to accumulate at DSBs to negatively regulate 53BP1 (58,59); however little is known about its role in the DDR. ATAD2 binds *in vitro* to hyperacetylated histone H4 tails through its bromodomain (60), and it is transcriptionally induced by anti-cancer and DNA-damaging agents via ATM and ATR checkpoint kinases. Silencing of ATAD2 sensitizes triple-negative breast cancer cells to carboplatin treatment (61) and it has been proposed to modulate BRCA1 activation, thereby acting on HR (62).

As derived from the TCGA database, both TPX2 and ATAD2 are overexpressed or amplified in aggressive tumors (Figure 4B), and high levels of ATAD2 correlate with poor prognosis especially in breast and kidney cancer (Figure 4C). These observations, together with the fast chromatin recruitment of both ATAD2 and TPX2 at γH2AX sites upon DSB induction, prompted us to further elucidate their role in DSB repair. Knockdown of either target resulted in a significant impairment in γH2AX foci formation and repair

(Figure 4D and Supplementary Figure S4B,C). In particular, while ATAD2-deficient cells failed to mount a correct early DSB response, depletion of TPX2 resulted in a progressive accumulation of unrepaired DSBs (Figure 4D and Supplementary Figure S4C). To further address their role in DSB repair, we adopted the U2OS-TLR cell system and confirmed HR deficiency upon ATAD2 depletion. Moreover, we observed a dramatic impairment of over 50% in homologous recombination efficiency also upon TPX2 silencing (Figure 4E and Supplementary Figure S4D,E). Notably, the severity of the effect almost reaches the level observed upon depletion of the hallmark of HR repair proteins RPA and RAD51 (Figure 2B). We therefore tested whether knockdown of ATAD2 or TPX2 could confer synthetic lethality in a combined treatment with PARPi (Figure 4F). Our results show that cells deficient for either target were sensitive to PARPi, thus validating their role in HR-mediated DSB repair. Interestingly, this effect was synergistic with etoposide treatment in TPX2- but not in ATAD2-depleted cells (Figure 4F), thereby implying that these two candidates might play a different role in the HR cascade. Indeed, while knockdown of either ATAD2 or TPX2 affected the formation of induced RAD51 foci (Figure 4G and Sup-

plementary Figure S4H), in contrast with previous reports (62) downregulation of ATAD2 did not affect BRCA1 foci formation and resolution. While in line with the reported interaction with the cell cycle regulator Aurora kinase A (AURKA) (59), TPX2 silencing resulted in a pronounced accumulation of cells in G2/M phase and a significant increase of BRCA1 foci (Figure 4H and Supplementary Figure S4F, G, I).

Collectively, we identified ATAD2 and TPX2 as novel interactors of γH2AX, and provide evidence for their key role in HR-mediated repair. Moreover, given that downregulation of either ATAD2 or TPX2 confers synthetic lethality to PARPi treatment, both these candidates might represent promising drug targets for combined treatment in HR-proficient cells.

Characterization of DNA repair-induced chromatin dynamics through isolation of protein on chromatin (iPOC)

ChIP-SICAP experiments represent a candidate approach, which require *a priori* knowledge about the target protein used as a bait in order to enrich for associated chromatin proteins. To complement the targeted view we obtained for γH2AX, RPA, RAD50 and MDC1, we aimed at extending this vision by developing an innovative and unbiased approach to determine DSB-induced changes in overall DNA-bound protein composition. Similar to recent strategies developed to study proteins interacting with nucleic acids (63–68), we exploited the use of nucleotide mimetics as a tool to mark the DNA, leaving a chemical trace amenable for the selective isolation of protein on chromatin (or iPOC). In particular, we labeled the DNA via full incorporation of 5-ethynyl-2′-deoxyuridine (EdU) for subsequent capture via copper-catalyzed azide-alkyne cycloaddition (CuAAC) of biotin azide (Figure 5A and Supplementary Figure S5A, B). Moreover, we combined this methodology with triple SILAC protein labeling and mass spectrometry to precisely quantify changes in the chromatin composition during the DDR. Specifically, medium- or heavy-labeled cells were subjected to EdU labeling and then either left untreated or collected at different time points (i.e. 1, 4 and 8 h) after DSB induction by IR, respectively. Light-SILAC cells were not subjected to EdU labeling and served as negative control. At each time point, crosslinked cells from the three differently SILAC-labeled samples were mixed in equal amounts and subjected to click chemistry-based biotin binding; chromatin was then sheared and DNA-bound proteins were enriched by means of protease-resistant streptavidin beads (or prS) (26). Upon tryptic digestion and mass spectrometry analysis, we therefore characterized the dynamics of DNA-bound chromatome during DSB repair (Figure 5B). To our knowledge, it is the first time that a similar approach has been employed in a quantitative and time course manner to describe global changes in chromatin composition.

Protein quantification showed the efficient and highly reproducible enrichment ($\geq$0.85) of DNA-binding proteins identified in EdU-treated samples over the negative control (Supplementary Figure S5C,D). Moreover, the high Spearman correlation ($>$0.6) between protein abundances at different time points indicates that iPOC is a very sensitive strategy that enables capturing the highly dynamic na-

ture of chromatin during the DSB response (Supplementary Figure S5E). To further assess the sensitivity, we benchmarked iPOC against deeply fractionated chromatin input where almost 4000 proteins were profiled during the DSB response (Supplementary Figure S5F, G). iPOC quantified almost 200 proteins that were either not identified in any of the ChIP-SICAP experiments or that were exclusively enriched in iPOC (i.e. 129 and 66 proteins, respectively) (Figure 5C, Supplementary Item S2). These results strongly highlight the orthogonality between the investigation of DNA-binding determinants associated with a target protein involved in DSB repair, and the unbiased dissection of chromatin regulation during DNA repair. Interestingly, iPOC-specific proteins were mainly enriched in gene ontology terms involved in chromatin organization, DSB repair and chromatin post-translational modification, thus further stressing the functional role of determinants exclusively quantified by iPOC (Figure 5D). In line with this, different classes of proteins associated with histone, transcription, chromatin regulation, DNA damage repair, and post-translational modification (i.e. ubiquitin) were overrepresented in iPOC in comparison with the chromatin input (Figure 5E), thereby indicating the high specificity of iPOC in enriching DNA-binding proteins. Accordingly, while proteins deregulated during the DSB response in the chromatin input were mainly involved in RNA processing and cell cycle (Supplementary Figure S5H,I), candidates quantified in iPOC at 1, 4 or 8 h time points were enriched in GO terms associated with DNA repair and chromatin organization (Figure 5F). In addition, the vast majority of proteins identified in iPOC were either not detected or not significantly deregulated in the chromatin input (Figure 5G and Supplementary Figure S5J), indicating that enrichment of chromatin-bound proteins *via* iPOC enhances sensitivity in detecting the dynamics of chromatin-associated proteins.

In iPOC we identified the DSB-induced DNA recruitment of different classes of epigenetic regulators ranging from histone modifying enzymes, to structural and core components of molecular machineries regulating the DDR. Moreover, in contrast to the chromatin input, in iPOC we observed the chromatin enrichment for candidates identified via ChIP-SICAP experiments such as MDC1, 53BP1, BRG1, NuMA, ATAD2 and TPX2. This result further corroborates the DSB-mediated chromatin association of novel candidates, while highlighting the sensitivity and specificity of our approach in detecting expected known DSB markers. For example, iPOC identified DNA repair proteins that associate with chromatin upon IR such as the topoisomerase II B (TOP2B), the telomeric repeat-binding factor TERF2 and the NHEJ regulator RIF1 (Figure 5G). Interestingly, upon DSB induction, we observed that the majority of the proteins were recruited to chromatin at an early time point (1 h), but we also detected different dynamics ranging from enrichment at later time point (e.g. CEBPB, MECP2, SUV39H1, CBX1, SRCAP and CDKN2AIP), to sustained DNA-association during the DSB repair (e.g. PHF14). Moreover, we identified an overrepresentation of chromatin-modifying enzymes among iPOC-enriched proteins, including subunits of acetyltransferase complexes (e.g. MORF4L1, KAT7 and BRD1), the histone demethylase KDM2A, the hPTM reader and tran-
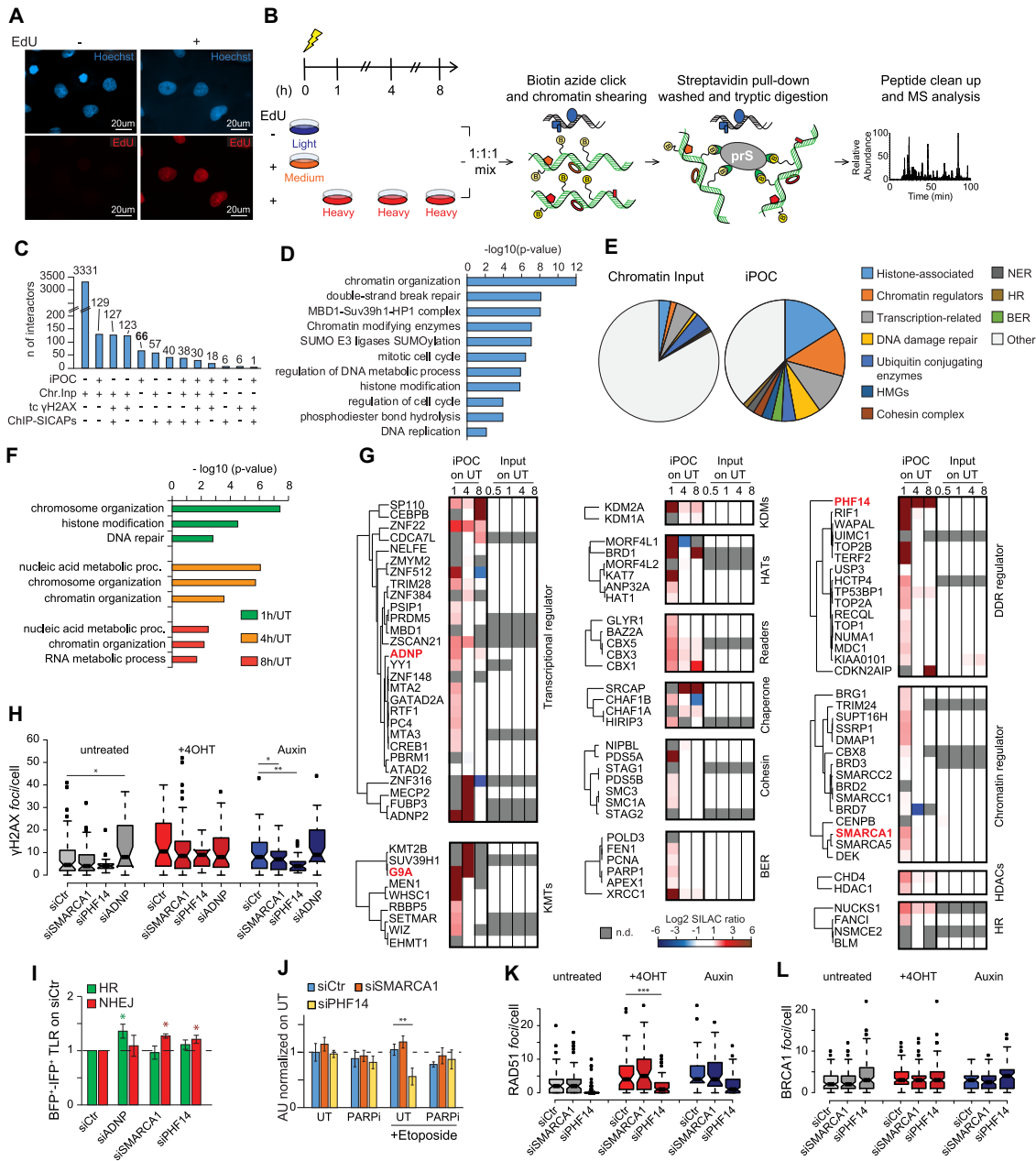
Figure 5. Chromatin composition dynamics during DDR investigated by iPOC. (**A**) Representative immunofluorescence of cells treated with DMSO (left) or the nucleotide analog EdU (right), and subjected to click chemistry with Alexa594-azide fluorophore. (**B**) Schematic representation of iPOC experimental strategy. SILAC labeled U2OS cells are exposed to either DMSO (light, as control) or EdU (medium and heavy) and crosslinked in untreated condition or at different time points during the DDR. Cells are then subjected to permeabilization, followed by click chemistry-based DNA labeling with biotin azide and enrichment with protease-resistant streptavidin beads (prS) prior to stringent washes, tryptic digestion and MS-based identification of chromatin-associated proteins. (**C**) Bar chart displays the overlap among functional interactors identified in ChIP-SICAP as from Figure 1 (ChIP-SICAPs), in time-course γH2AX-experiment from Figure 3 (tc γH2AX), in iPOC and in fractionated chromatin preparation used as input for ChIP (Chr.Inp). (**D**) Top 11 gene ontology categories associated with targets exclusively quantified in iPOC. (**E**) Comparison between the frequency of listed categories of protein in the fractionated chromatin input (Chromatin Input, left) and in iPOC (right). (**F**) Gene ontology (GO) categories associated with proteins identified in iPOC as recruited at chromatin at the different time points upon ionizing radiation (IR) compared with untreated condition. (**G**) Hierarchical clustering heatmap representation of SILAC ratios (in log2) for functional categories of DDR- and chromatin-regulators quantified in iPOC at different time points during DSB repair over untreated sample (UT). For all targets, the relative dynamics quantified in the fractionated chromatin input over the respective untreated condition (input on UT) is also shown. Proteins further followed up are highlighted in red; n.d.: not detected. (**H**) Number of γH2AX foci per nucleus in AID-DIvA cells after target knockdown upon DSB induction and repair (tamoxifen/+4OHT and Auxin, respectively), in comparison with on-target non-targeting silencing control (siCtr). (**I**) Quantification of HR (green) and NHEJ (red) repair events in U2OS-TLR cells depleted for ADNP, SMARCA1, or PHF14 and normalized on silencing control (siCtr). Green and red asterisks reflect significant regulation in HR and NHEJ, respectively, from siCtr. (**J**) Quantification of CFA in U2OS cells depleted of PHF14 or SMARCA1 and subjected to PARPi alone or in combination with etoposide to promote DSBs formation. Mean values of three biological replicates normalized to untreated condition (UT) with standard deviation are shown. Quantification of RAD51 (**K**) and BRCA1 (**L**) foci in AID-DIvA cells after target knockdown. *, ** and *** correspond to *P*-value < 0.05, 0.01 and 0.001 of ANOVA statistical test, respectively.

scriptional regulator PSIP/LEDGF, and the methyltransferases KMT2B/MLL4, WHSC1/NSD2, SETMAR and EHMT2/G9A (Figure 5G and Supplementary Figure S5J). Taken together, these results demonstrate the sensitivity of iPOC in capturing the DNA damage-induced dynamics even for proteins with very fast kinetics such as chromatin remodelers.

In addition, and in contrast to targeted approaches like ChIP-SICAP, iPOC has the inherent ability to investigate the overall histone composition in chromatin. Indeed, we observed that in the chromatin input the abundance of most histones declined upon IR, while this effect was generally less pronounced for DNA-bound histones identified through iPOC (Supplementary Figure S5K). Our data are therefore in line with the recently reported proteasome-mediated depletion of histones during DNA repair (69) but suggest that soluble histones might strongly contribute to this phenomenon. Even more interestingly, in iPOC we observed that changes in DNA-bound histones during DSB repair occurred in a time- and histone variant-specific manner, sometimes even leading to a transient increase (e.g. H1.4, H2A.1–3) (Supplementary Figure S5K). Although the iPOC approach is not specifically designed for the analysis of histone proteins, these results together with the dynamic recruitment of histone chaperones observed in iPOC (Figure 5G), suggest a possible mechanism to retain, evict or recruit distinct variants to potentially drive a chromatin conformation status amenable for the DSB repair process. Nevertheless, additional experiments are needed in order to further assess this hypothesis.

Collectively, the iPOC approach allows for the unbiased temporal characterization of the chromatin composition and the interplay among its regulators during DNA repair, thus providing an orthogonal view point to the candidate-approaches based on ChIP-SICAP. In addition, our data report a strong overrepresentation of chromatin modifying enzymes and proteins involved in post-translational modifications of histone and non-histone proteins, thereby highlighting the sensitivity of the methodology in capturing the dynamic enrichment of transient chromatin interactors.

ADNP, SMARCA1 and PHF14 are novel chromatin-associated proteins with distinct functions in DSB repair

Among the candidates identified exclusively via iPOC as recruited at chromatin, we selected three targets belonging to different functional groups to assess their potential role in DNA damage repair (Figure 5G). In particular, we focused on two negative prognostic markers in cancer, ANDP and PHF14 (70,71), and a chromatin regulator, SMARCA1/SNF2L (72). We first evaluated the formation and repair efficiency of γH2AX foci in cells after knockdown of these targets (Supplementary Figure S5L). We observed that silencing of ADNP increased the number of foci already in untreated conditions, resulting in the accumulation of unrepaired DSBs (Figure 5H and Supplementary Figure S5M). Recent evidence showed that ADNP, together with CHD4 and HP1, forms the ChAHP remodeling complex involved in the regulation of higher-order chromatin structure (73). The DSB-induced recruitment of CHD4 observed in iPOC might therefore point toward a

possible role of this complex in genome stability, but we cannot exclude a separate function of ADNP during the DDR. In agreement with our observation on the role of ADNP in DSB repair and similarly to silencing of HMGA2 (Figure 2B), depletion of ADNP in U2OS-TLR cells significantly promotes HR (Figure 5I and Supplementary Figure S5N,O), an effect that was not caused by cell cycle deregulation (Supplementary Figure S5P, Q). Our data support a novel role for ADNP in DSB repair, although additional experiments are needed to further investigate the increased number of γH2AX foci observed in untreated condition upon ADNP depletion (Figure 5H). In contrast, similar experiments demonstrated that SMARCA1 and PHF14 are both involved in preventing NHEJ repair as their silencing increases the fraction of end-joining events (Figure 5I and Supplementary Figure S5N,O). Although we cannot exclude a direct role of PHF14 silencing leading to a significant reduction of γH2AX foci in untreated condition, our results show how PHF14-deficient cells are able to normally respond to DSBs induction (Supplementary Figure S5M). We therefore suggest that upon depletion of either PHF14 or SMARCA1, the higher rate of the fast end-joining repair might explain the lower number of unrepaired γH2AX foci (i.e. Auxin-treated sample) in comparison with silencing control (Figure 5H). Accordingly, silencing of neither SMARCA1 nor PHF14 promoted synthetic lethality with PARPi, as observed upon depletion of TRA2B, which is similarly involved in the inhibition of NHEJ (Figure 2E).

Interestingly, although having an analogous role in DNA repair, PHF14 and SMARCA1 seem to follow a different kinetics at chromatin, suggesting a potential non-redundant function. Indeed, depletion of PHF14 sensitized cells to the chemotherapeutic agent etoposide and caused defective formation of RAD51 foci (Figure 5J,K and Supplementary Figure S5R), corroborating recent findings (74). In contrast, we did not observe a significant impact of SMARCA1 depletion on either RAD51 or BRCA foci (Figure 5K, L and Supplementary Figure S5R,S), thus suggesting a more structural role for the core component of the Nucleosome remodeling factor (NuRF) during DSB repair.

In summary, iPOC identified multiple proteins that associate with DNA upon DSB, and the functional characterization of selected candidates (e.g. SMARCA1, PHF14 and ADNP) provide evidence for their involvement and mechanism in the DDR, thus highlighting the discovery power of this methodology.

Dynamics of hPTMs in chromatin and at DSB-sites during DNA damage repair

The overrepresentation of chromatin-modifying enzymes, in particular methyltransferase observed in iPOC (Figure 5G), together with their established fundamental function in DNA damage repair (75), prompted us to investigate histone PTMs as an additional regulatory layer that impinges on chromatin stiffness and accessibility. In particular, we employed Native Chromatin Proteomics (N-ChroP) (27,28) in a time-course manner to globally characterize the dynamic changes of hPTMs during the DDR (hereafter termed DDR-induced hPTMs) with single nucleosome resolution. In parallel, we profiled temporal trends of histone

modifications specifically at γH2AX-containing mononucleosomes (henceforth foci-specific hPTMs).

To achieve this goal, we prepared mononucleosomes from U2OS cells at different time points during IR-induced DSB repair and we profiled the hPTM-dynamics via the ArgC-like in-gel digestion prior to mass spectrometry analysis (Figure 6A and Supplementary Figure S6A,B). For each hPTM, we described its relative abundance (RA) compared with the amount of concomitant modifications on the same peptide, and the relative enrichment (RE) corresponding to the fold enrichment between the RA of a certain modification in γH2AX-mononucleosomes and in the native chromatin mononucleosomes preparation (i.e. input) (Figure 6A). As a result, we identified 33 different histone modifications on 14 peptides from histone H2A, H3 and H4, and we quantified their temporal abundance during DSB repair (Figure 6B, Supplementary Figure S6C–E, Supplementary Item S3). In particular, the identified modifications not only span the well-characterized N-terminal histone 'tail', but we also robustly profiled hPTMs in the core region of each histone protein. Moreover, we quantified modifications with different dynamic range from more frequent to sub-stoichiometric hPTMs. To our knowledge, this represents the first example of extensive and unbiased temporal profiling of hPTMs during the DDR with single-nucleosome resolution.

In order to avoid sample biases and to shorten the handling, we focused our investigation on hPTM that do not require additional enrichment steps. Our analyses indicate that, as shown by the relative enrichment of hPTMs (RE), already in untreated conditions γH2AX-mononucleosomes have a distinct hPTM pattern, being enriched for hyperacetylated in the N-terminal tail of histone H4, a modification associated with open chromatin state (76), and monomethylated lysine 20 on histone H4 (H4K20me1) (Figure 6B), a known hPTM with a pivotal role in DSB repair (77,78). These results suggest that γH2AX-containing nucleosomes may be inherently enriched in modifications that establish a more relaxed chromatin state, to potentially promote accessibility for the repair machinery and thus 'prime' for DNA damage repair signaling. As an alternative explanation, open chromatin domains could possibly be more prone to spontaneous DSBs in unperturbed condition.

In addition to providing the composition of γH2AX-mononucleosomes at steady-state, our analysis allows distinguishing with very high resolution hPTMs that are globally induced upon DSB (DDR-induced), from modifications acquired exclusively in mononucleosomes in close proximity to the break site and marked by γH2AX (foci-specific). Among the DDR-induced hPTMs, we identified that dimethylated K79 on histone H3 (H3K79me2) has a bimodal enrichment at 30 min and 4 h (Figure 6B and Supplementary Figure S6D). The abundance of this modification positively correlates with transcription rate (79), moreover this hPTM can supposedly act as docking site for the chromatin recruitment of 53BP1 (80). The synchronous DSB-mediated increase of this modification in both native chromatin input and in γH2AX-mononucleosomes, suggests that H3K79me2 might globally promote the transcription of DNA repair genes, while at DSB sites it could stimulate the production of DDR-induced RNAs or recruit

53BP1. In the same class of modifications, we interestingly identified that K95 of histone H2A (H2AK95) is globally monomethylated during DNA damage repair and accumulates at late time points along the repair (Figure 6B and Supplementary Figure S6C). Although little is known about the functional role of modifications on this core histone residue (81,82), our results suggest involvement of H2AK95me1 in the DDR signaling.

Recent efforts have been dedicated to the investigation of foci-specific hPTMs, the most successful advance relies on the intersection between breaks-labeling and sequencing (BLESS) profiles and ChIP-sequencing tracks of *a priori* selected hPTMs (16,83). While ChIP distinguished *a priori* selected hPTMs enriched at NHEJ- and HR-prone DSBs, this approach falls short in exploring unpredicted modifications and in studying their combinatorial occurrence. Our proteomic-based approach circumvents these limitations by the quantitative, unbiased and simultaneous analysis of multiple hPTMs. Indeed, at γH2AX-mononucleosomes we observed an increase in mono- and di-methylation on K20 of histone H4 (H4K20me1 and H4K20me2) (Figure 6B and Supplementary Figure S6E), two modifications with a pivotal role in DSB repair pathway choice (22–24). In particular, our time-course analysis showed different kinetics between mono- and di-methylation, where H4K20me1 precedes the dimethylation, enriched at later time points during DSB repair. This effect could either be due to the sequential recruitment of SETD8 and SUV40H1/2 required for achieving a higher methylation degree, or potentially to a different role of H4K20me1 and H4K20me2 in the DDR cascade.

Encouraged by the characterization of dynamics for expected hPTMs at break sites, we expanded our analysis to unexpected trends during the DDR. Among the foci-specific hPTMs we observed a progressive increase of monomethylation of K18 and acetylation of K64 on histone H3 (H3K18me1 and H3K64Ac, respectively) (Figure 6B and Supplementary Figure S6D). Monomethylation of H3K18 is mutually exclusive with the acetylation on the same residue and it has been associated with silencing chromatin (84). In DNA repair, H3K18 needs to be deacetylated through SIRT7 to allow 53BP1 recruitment at DSBs, therefore our results suggest that H3K18me1 is a rapid and possibly important mediator of NHEJ repair. In contrast, H3K64Ac is enriched at actively transcribed regions (85), therefore its gradual increase during the DDR observed at γH2AX mononucleosomes might promote local chromatin relaxation and DDR-induced histone exchange (Figure 6B and Supplementary Figure S6D). Taken together, we employed an innovative strategy to characterize dynamic profiles of 33 hPTMs. In particular, we distinguished DSB-induced kinetic profiles of hPTMs that occur globally from those marked by γH2AX, to causally associate hPTMs with DSB events at mono-nucleosome resolution.

Integrative chromatin proteomics implicates G9A-mediated H3K56me1 in the DDR

The added value of our multi-layered approach resides in the integration of the complementary chromatin data to derive functional causality, and to infer novel aspects of the

Figure 6. Profiling of hPTMs during DDR at mononucleosome resolution. (**A**) Experimental design of time course N-ChroP. Mononucleosomes from cells at different time points during the DDR (hour post irradiation) are enriched for γH2AX and associated hPTMs are quantified via MS upon chemical derivatization and tryptic digestion (ArgC-like digestion). For each hPTM the RA is calculated as the extracted ion chromatography (XIC) of a specific modification over the sum of XICs for all modifications occurring on the same peptide. The RE of each hPTM represents the ratio between its RA in the enriched ChIP over the RA in the mononucleosome input. (**B**) Heatmap representation of the log2 RA for hPTMs in γH2AX-enriched mononucleosomes (γH2AX) or in native mononucleosome preparation used as input (Input) calculated over the respective untreated sample (UT). Relative enrichment at steady state (RE UT) highlights the specific combinatorial patterns of hPTMs at γH2AX-marked mononucleosomes. DDR-induced and foci-specific modifications are highlighted in green and light blue, respectively. Abundance relative to UT conditions for writers (red), erasers (blue) or readers (green) associated with H3/H4 acetylation (**C**), H4K20me2 (**D**), H3K36me2/me3 (**E**) and H3K56me1 (**F**). Lines correspond to protein abundance in fractionated chromatin input (Chr.Inp, left) or in iPOC (right). Heatmap represents RA of hPTM during DSB repair in the native chromatin input (native chromatin, left) or in γH2AX-marked mononucleosomes (γH2AX-mononucleosomes, right). (**G**) Quantification of HR (green) and NHEJ (red) repair events in U2OS-TLR cells upon inhibition of G9A (G9Ai) normalized to silencing control (siCtr). Green asterisk reflects significant regulation in HR compared with siCtr. (**H**) Quantification of CFA in U2OS cells upon G9A inhibition and subjected to PARP inhibitor (PARPi) alone or in combination with etoposide treatment. Mean values normalized to untreated condition (UT) and standard deviations are shown. Quantification of RAD51 (**I**) and BRCA1 (**J**) foci in AID-DIvA cells upon drug-inhibition of G9A (G9Ai). ** and *** in panel H-J correspond to *P*-value < 0.01 and 0.001 of ANOVA statistical test, respectively; n.s. = not significant, UT = untreated conditions, +4OHT = upon DSB formation, Auxin = resolution of DNA breaks.

DSB repair. In particular, we profiled chromatin-associated abundance for different histone writers, erasers and readers during DSB repair determined by iPOC (Figure 5G) and integrated this with the kinetic profiles of their cognate DDR-induced and foci-specific hPTMs (Figure 6B). The overlay shows that the chromatin recruitment for both writer and eraser of H3 and H4 acetylation (i.e. KAT7 and HDAC1, respectively) observed in iPOC, seems to be responsible for DDR-induced hPTM dynamics. In particular, decreased acetylation on H3 coincides with an increased HDAC1 chromatin association, while the transient increase in both KAT7 and H4 di-acetylation suggest a functional link (Figure 6C and Supplementary Figure S6D,E). We could also link the kinetics of histone readers and their foci-specific hPTM, including the well-known crosstalk between dimethylated K20 on histone H4 (H4K20me2) and 53BP1, which drives toward NHEJ (Figure 6D and Supplementary Figure S6E). In line with the replication-coupled dilution model (23), our findings suggest a rapid end joining-mediated repair of the DSBs, followed by a chromatin depletion of both these determinants at later time points of the repair process. The prolonged 53BP1 chromatin association in comparison with H4K20me2 may reflect the resolution difference between N-ChroP and iPOC (mononucleosomes and ± 500 bp, respectively), or might be required for the proper recruitment of the NHEJ machinery (i.e. 53BP1-RIF1-Shieldin axis). In addition, among the foci-specific hPTM, we observed a rapid increase of di- and tri-methylated K36 on histone H3 (i.e. H3K36me2 and H3K36me3) that is fully compatible with the chromatin enrichment observed in iPOC for SETMAR and PSIP1, which are the respective writer of H3K36me2 and reader of H3K36me3 (Figure 6E and Supplementary Figure S6D). In contrast, the DSB-mediated chromatin recruitment of KDM2A seems to be decoupled from the methylation state of H3K36 (Figure 6E).

The identification of known crosstalk between chromatin regulators and their cognate hPTMs, prompted us to expand our investigation to unexpected pairing between such determinants. In line with previous reports (86,87), we observed the fast chromatin recruitment of the methyltransferase G9A upon DSBs formation. This target caught our attention in light of the concomitant foci-specific increase of monomethylation of its target residue K56 of histone H3 (H3K56me1) (Figure 6F). H3K56 is located on the lateral surface of histone H3 close to DNA entry/exit site, and its acetylation seems to contribute to chromatin reassembly after DNA repair, while a role in cell cycle progression has been proposed for H3K56me1 (88,89). Our data reveal that, in mononucleosomes flanking the break site, G9A-mediated monomethylation precedes the acetylation of H3K56 (1 and 4 h) (Figure 6B,F and Supplementary Figure S6D,G), thus providing for the first time a role for H3K56me1 in the DDR. In the functional investigation of this novel epigenetic crosstalk, we examined and observed that differently from the suggested role in NHEJ (90), inhibition of G9A with the selective inhibitor BIX-01294 dramatically decreased the efficiency of HR without perturbing cell cycle regulation (Figure 6G and Supplementary Figure S5N–Q). In line with these results, inhibition of G9A sensitized to treatment with PARPi alone or in combina-

tion with etoposide (Figure 6H). In particular, the selective inhibition of G9A decreased the number of RAD51 foci in untreated condition but did not affect its chromatin recruitment upon DSBs induction; moreover G9Ai resulted in a significant increase in BRCA1 loading at DSBs and deficient repair at these foci (Figure 6I,J and Supplementary Figure S5R,S). Interestingly, the interaction between H3K56me1 and γH2AX is mediated by the induction of DSBs, and decreases upon treatment with low concentrations of G9Ai that are not responsible for the global loss of H3K56me1 (Supplementary Figure S6F–H). Taken together, our results show that G9A is rapidly recruited to chromatin upon DSB, where it promotes monomethylation of H3K56 at γH2AX mononucleosomes. Since inhibition of G9A causes accumulation of BRCA1 foci and impairs homologous recombination repair, our data suggest that H3K56me1 may have a role in HR pathway, presumably by acting as docking site for proteins involved in HR repair downstream of BRCA1.

In summary, we showed how our multi-layered approach identified temporal dynamics shared between chromatin regulators and either cognate DDR-induced or DNA repair foci-specific modifications. Among the novel crosstalk identified, we further demonstrated the relationship between H3K56me1 and G9A in DNA damage, and showed that inhibition of this enzyme decreases HR repair efficiency and sensitizes BRCA-proficient cells to PARPi treatment, thus identifying a synthetic lethality with potential clinical relevance.

DISCUSSION

Double-strand break repair takes place in the context of chromatin, where a coordinated mechanism engages histone PTMs and DNA-recruited regulators to set the stage for the efficient damage response cascade (6). To clarify this dynamic and composite picture, here we characterized the response to DSB from a chromatin-centric perspective using three exploratory proteomic-based approaches. In detail, we investigate the chromatin organization at different levels of resolution, namely global DNA-bound proteome (studied by iPOC), functional interaction maps of DDR core components (in ChIP-SICAP) (25) and hPTMs at monucleosomes flanking the break site (in N-ChroP) (27). Moreover, by adding a temporal dimension, we generated complementary data sets that collectively produce a comprehensive and detailed panorama of the chromatin dynamics during the DDR. This rich resource, which can be mined in an interactive fashion (at https://chromatin-proteomics.dkfz.de/), led us to functionally characterize multiple proteins and hPTMs that had not been associated with DSB repair before, and assigned them a role in HR, NHEJ or pathway choice. In addition, for several unanticipated HR-associated proteins we identified synthetic lethality with PARPi in HR-proficient cells (HRDness or BRCAness), thus opening to clinically relevant opportunities.

iPOC is a novel approach that we developed to capture, identify and quantify proteins recruited to or evicted from chromatin during the DDR. Salient features of iPOC include DNA labeling by the thymidine analog EdU, as in iPOND and iPOTD (66,91), combined with SILAC la-
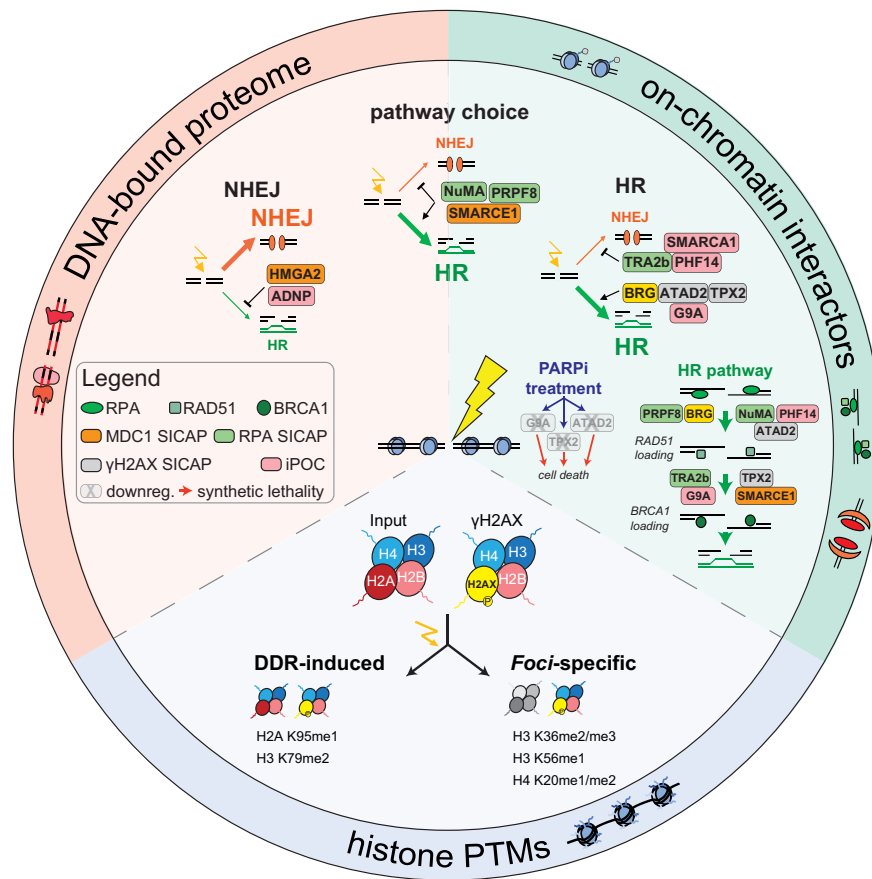
Figure 7. Multi-layered chromatin-directed proteomics identifies cell vulnerabilities in HR and NHEJ. Integration of orthogonal approaches in chromatin-directed proteomics identifies chromatin proteins contributing to NHEJ, repair pathway choice, and HR; moreover it distinguishes trends of hPTMs induced globally during the DNA damage repair (DDR-induced) from modifications specifically enriched at γH2AX-mononucleosomes (*foci*-specific). Orthogonal imaging-based strategies determine the role in the early steps of homologous recombination repair (HR pathway) for chromatin targets involved in either HR or pathway choice, while CFA assays identify targets whose downregulation drives towards synthetic lethality with PARPi epigenetic drug (PARPi treatment).

beling for robust protein quantification, and capture of biotinylated complexes on protease-resistant streptavidin beads (26) to boost assay sensitivity. Differently from iPOND and NCC (67) that offer a site-specific view, the power of iPOC resides in its ability to determine compositional changes on a chromatin-wide scale, thereby complementing more targeted approaches like ChIP-SICAP. Indeed, beyond identifying core repair proteins also found in ChIP-SICAP, multiple proteins were exclusively identified in iPOC, notably proteins known for having transient interactions with the DNA like chromatin-modifying enzymes and transcriptional regulators (Figure 5G). These data not only highlight the sensitivity of the approach but also underscore the simultaneous recruitment of functionally diverse sets of proteins and suggest that their respective biological activities cannot be seen in isolation. As an illustrative example, we showed cross-regulation among functional processes through the negative modulation of HR mediated by the transcriptional regulator ADNP (Figure 5I). Here, we applied iPOC to the DDR, however, we envision that, in replicating cells, this approach can be extended to characterize changes in overall chromatin composition upon any molecular or cellular perturbation.

Another unique aspect of our study is the discrimination between DDR-induced and DNA repair foci-specific hPTMs by N-ChroP. Indeed, this approach brings together the unbiased nature of mass spectrometry-based proteomics with the specificity of ChIP to characterize hPTMs landscape of a specific chromatin region. In comparison with widely used ChIP-seq approaches (16), N-ChroP identifies cross-talks among hPTMs without *a priori* knowledge beside the modification of interest. Applied in a time-course fashion, this allowed us to confirm known and reveal novel PTM profiles, and to provide a refined view to published data. For instance, H3K79 acts as one of the docking sites for 53BP1 recruitment (79); however, its methylation level has been reported to be unchanged or to decrease upon DSB (16,92). Our dynamic data show that H3K79me2 follows a bi-modal increase at 0.5 and 4 h from DSB induction (Figure 6B and Supplementary Figure S6D), while this modification is partially depleted at foci-specific level at 8 h after IR, thus indicating that the time of sampling is crucial to explain these apparently conflicting observations. Similarly, H3K56Ac has been reported to be either deregulated or unchanged in the DDR (93). Our results may clarify these conflicting reports as we observed a foci-specific in-

crease at late time points during DSB repair, accompanied by a decrease of this modification on a global scale (Figure 6B and Supplementary Figure S6D), thus pointing to a resolution-dependent dynamics.

Since our proteomic approaches characterize complementary chromatin layers, their integration offers a detailed view to better understand the DNA repair process. Cross-correlation of these data may not prove direct causality; however, they provide compelling examples of regulatory events such as between hPTMs and their cognate writers and readers. For instance, the overlay of N-ChroP and iPOC data indicate the cross-talk among the methyltransferase SETMAR, the reader PSIP and the foci-specific increase in trimethylated H3K36. Similarly we also identified coinciding temporal profiles between the hyper-acetylation of 9–17 peptide of histone H3 and the enrichment at chromatin for the histone acetyltransferase responsible for H3K14 acetylation KAT7; similarly also the chromatin dynamics of 53BP1 and dimethylated H4K20, a modification well-known to be involved in DSB repair regulation (22,23) (Figures 5G, 6B–F). Notably, we focused our attention on the chromatin recruitment of G9A, an enzyme that can methylate H3K9 and H3K56. In our previous work, we could readily detect H3K9me2/3 (28), while we were unable to identify these hPTMs during the DDR. We therefore conclude that di- and tri-methylation of H3K9 occur at undetectable levels or do not correlate particularly with DNA damage, in agreement with recent data showing a lack of association between H3K9me2/3 and DSB repair (16). Interestingly however, we instead observed a foci-specific increase of monomethylated H3K56, another substrate of G9A, thus suggesting a functional link between G9A recruitment and H3K56me1. Moreover, induction of HRDness upon G9A inhibition (Figure 6H–I) in the absence of H3K9me2/3 suggests that, besides its function in DNA replication (89), H3K56me1 might have an as-yet unrecognized role in HR downstream of BRCA1. This illustrates how our complementary results represent a valuable resource to describe the complexity of chromatin response to DSBs (Figure 7) and to propose a possible mechanism of action for newly identified DSB-dependent chromatin proteins.

Through ChIP-SICAP and iPOC we identified novel candidates involved in the DDR, which we characterized by means of the traffic light reporter assay allowing for the monitoring of both NHEJ and HR events in the same cell population (38). This DSB cell system was fundamental especially to distinguish DDR components regulating both pathways (e.g. NuMA, SMARCE1 and PRPF8) from chromatin proteins exclusively involved in HR (e.g. ATAD2, TPX2 and G9A). Importantly, while both classes of proteins exhibit an overall decrease in HR efficiency, only the latter group shows sensitization to PARPi treatment (Figures 2B, E, 4E, F, 6G, H).

These findings demonstrate that our multi-layered chromatin approach powerfully complements genetic screens to identify HRDness, while potentially explaining the benefit of PARPi-therapy observed in BRCA wild-type patients (94,95). In addition, newly identified chromatin regulators involved in DSB repair may be nominated as promising drug targets, spurring ongoing efforts to develop epige-netic drugs for targeted therapies or in combination with PARPi (96). Indeed, when looking for synthetic lethality, we could shortlist various targets to be investigated in knock-down screens; moreover the functional interaction identified via our chromatin-centered proteomics might mimic genetic interaction and suggest cooperativity between or among identified targets. Such data could also be a valuable resource for multigene perturbation technologies (97) to identify paralogues or functionally related proteins that may be a suitable target for such multiple knockdown approaches.

Our chromatin-directed analysis suffers from limitations in common with other proteomic-based strategies. First, these data do not indicate the chromatin conformation and the genomic localization of the described interactions. Second, iPOC and N-ChroP describe associations among chromatin determinants without discriminating between NHEJ- or HR-prone sites. Therefore, affinity-based enrichment of candidates coupled with sequencing represents the optimal orthogonal validation for both these aspects. Finally, so far we only explored a few classes of PTM and focused almost exclusively on histones without investigating modifications on non-histone proteins. For this reason, on the same line as previous studies (98), further multi-layered studies examining PTMs on other chromatin proteins will be complementary to our data.

In line with the idea of multi-omics integration (99), our findings show how multiple chromatin-centered approaches are needed to describe the complexity of biological processes such as DNA damage repair. At the same time the temporal dimension is fundamental for defining the protein dynamics via unbiased approaches like mass spectrometry. To the best of our knowledge, this strategy represents the first resource of chromatin-mediated functional interactions during DNA repair, and provides a focused yet comprehensive view of this biological process.

RESOURCE AVAILABILITY

Lead contact

Further information and requests for resources and reagents should be directed to and will be fulfilled by the lead contact, Prof. Jeroen Krijgsveld (j.krijgsveld@dkfz.de).

Materials availability

This study did not generate new unique reagents.

DATA AVAILABILITY

The webpage-based viewer for the experiments described in this manuscript is available at 'https://chromatin-proteomics.dkfz.de/'.

The mass spectrometry proteomics data have been deposited to the ProteomeXchange Consortium via the PRIDE (https://www.ebi.ac. uk/pride/) (42) partner repository with the dataset identifier PXD027421.

The ChIP-SICAP protocol is maintained at protocols.io: dx.doi.org/10.17504/protocols.io.bcrriv56.

REFERENCES

1. San Filippo,J., Sung,P. and Klein,H. (2008) Mechanism of eukaryotic homologous recombination. *Annu. Rev. Biochem.*, **77**, 229–257.
2. Huertas,P. (2010) DNA resection in eukaryotes: deciding how to fix the break. *Nat. Struct. Mol. Biol.*, **17**, 11–16.
3. Harper,J.W. and Elledge,S.J. (2007) The DNA damage response: ten years after. *Mol. Cell*, **28**, 739–745.
4. Jackson,S.P. and Bartek,J. (2009) The DNA-damage response in human biology and disease. *Nature*, **461**, 1071–1078.
5. Probst,A.V., Dunleavy,E. and Almouzni,G. (2009) Epigenetic inheritance during the cell cycle. *Nat. Rev. Mol. Cell Biol.*, **10**, 192–206.
6. Green,C.M. and Almouzni,G. (2002) When repair meets chromatin. First in series on chromatin dynamics. *EMBO Rep.*, **3**, 28–33.
7. Scully,R., Panday,A., Elango,R. and Willis,N.A. (2019) DNA double-strand break repair-pathway choice in somatic mammalian cells. *Nat. Rev. Mol. Cell Biol.*, **20**, 698–714.
8. Ceccaldi,R., Rondinelli,B. and D'Andrea,A.D. (2016) Repair pathway choices and consequences at the double-strand break. *Trends Cell Biol.*, **26**, 52–64.
9. Lord,C.J. and Ashworth,A. (2016) BRCAness revisited. *Nat. Rev. Cancer*, **16**, 110–120.
10. Pilie,P.G., Tang,C., Mills,G.B. and Yap,T.A. (2019) State-of-the-art strategies for targeting the DNA damage response in cancer. *Nat. Rev. Clin. Oncol.*, **16**, 81–104.
11. Boeing,S., Williamson,L., Encheva,V., Gori,I., Saunders,R.E., Instrell,R., Aygun,O., Rodriguez-Martinez,M., Weems,J.C., Kelly,G.P. *et al.* (2016) Multiomic analysis of the UV-Induced DNA damage response. *Cell Rep.*, **15**, 1597–1610.
12. Haahr,P., Hoffmann,S., Tollenaere,M.A., Ho,T., Toledo,L.I., Mann,M., Bekker-Jensen,S., Raschle,M. and Mailand,N. (2016) Activation of the ATR kinase by the RPA-binding protein ETAA1. *Nat. Cell Biol.*, **18**, 1196–1207.
13. Raschle,M., Smeenk,G., Hansen,R.K., Temu,T., Oka,Y., Hein,M.Y., Nagaraj,N., Long,D.T., Walter,J.C., Hofmann,K. *et al.* (2015) DNA repair. Proteomics reveals dynamic assembly of repair complexes during bypass of DNA cross-links. *Science*, **348**, 1253671.
14. Gupta,R., Somyajit,K., Narita,T., Maskey,E., Stanlie,A., Kremer,M., Typas,D., Lammers,M., Mailand,N., Nussenzweig,A. *et al.* (2018) DNA repair network analysis reveals shieldin as a key regulator of NHEJ and PARP inhibitor sensitivity. *Cell*, **173**, 972–988.
15. Schep,R., Brinkman,E.K., Leemans,C., Vergara,X., van der Weide,R.H., Morris,B., van Schaik,T., Manzo,S.G., Peric-Hupkes,D., van den Berg,J. *et al.* (2021) Impact of chromatin context on Cas9-induced DNA double-strand break repair pathway balance. *Mol. Cell*, **81**, 2216–2230.
16. Clouaire,T., Rocher,V., Lashgari,A., Arnould,C., Aguirrebengoa,M., Biernacka,A., Skrzypczak,M., Aymard,F., Fongang,B., Dojer,N. *et al.* (2018) Comprehensive mapping of histone modifications at DNA double-Strand breaks deciphers repair pathway chromatin signatures. *Mol. Cell*, **72**, 250–262.
17. Downs,J.A., Allard,S., Jobin-Robitaille,O., Javaheri,A., Auger,A., Bouchard,N., Kron,S.J., Jackson,S.P. and Cote,J. (2004) Binding of chromatin-modifying activities to phosphorylated histone H2A at DNA damage sites. *Mol. Cell*, **16**, 979–990.
18. Jha,S., Shibata,E. and Dutta,A. (2008) Human Rvb1/Tip49 is required for the histone acetyltransferase activity of Tip60/NuA4 and for the downregulation of phosphorylation on H2AX after DNA damage. *Mol. Cell. Biol.*, **28**, 2690–2700.
19. Kusch,T., Florens,L., Macdonald,W.H., Swanson,S.K., Glaser,R.L., Yates,J.R. 3rd, Abmayr,S.M., Washburn,M.P. and Workman,J.L. (2004) Acetylation by Tip60 is required for selective histone variant exchange at DNA lesions. *Science*, **306**, 2084–2087.
20. Murr,R., Loizou,J.I., Yang,Y.G., Cuenin,C., Li,H., Wang,Z.Q. and Herceg,Z. (2006) Histone acetylation by Trrap-Tip60 modulates loading of repair proteins and repair of DNA double-strand breaks. *Nat. Cell Biol.*, **8**, 91–99.
21. Botuyan,M.V., Lee,J., Ward,I.M., Kim,J.E., Thompson,J.R., Chen,J. and Mer,G. (2006) Structural basis for the methylation state-specific recognition of histone H4-K20 by 53BP1 and Crb2 in DNA repair. *Cell*, **127**, 1361–1373.
22. Saredi,G., Huang,H., Hammond,C.M., Alabert,C., Bekker-Jensen,S., Forne,I., Reveron-Gomez,N., Foster,B.M., Mlejnkova,L., Bartke,T. *et al.* (2016) H4K20me0 marks post-replicative chromatin and recruits the TONSL-MMS22L DNA repair complex. *Nature*, **534**, 714–718.
23. Pellegrino,S., Michelena,J., Teloni,F., Imhof,R. and Altmeyer,M. (2017) Replication-coupled dilution of H4K20me2 guides 53BP1 to pre-replicative chromatin. *Cell Rep.*, **19**, 1819–1831.
24. Simonetta,M., de Krijger,I., Serrat,J., Moatti,N., Fortunato,D., Hoekman,L., Bleijerveld,O.B., Altelaar,A.F.M. and Jacobs,J.J.L. (2018) H4K20me2 distinguishes pre-replicative from post-replicative chromatin to appropriately direct DNA repair pathway choice by 53BP1-RIF1-MAD2L2. *Cell Cycle*, **17**, 124–136.
25. Rafiee,M.R., Girardot,C., Sigismondo,G. and Krijgsveld,J. (2016) Expanding the circuitry of pluripotency by selective isolation of chromatin-associated proteins. *Mol. Cell*, **64**, 624–635.
26. Rafiee,M.R., Sigismondo,G., Kalxdorf,M., Forster,L., Brugger,B., Bethune,J. and Krijgsveld,J. (2020) Protease-resistant streptavidin for interaction proteomics. *Mol. Syst. Biol.*, **16**, e9370.
27. Soldi,M. and Bonaldi,T. (2013) The proteomic investigation of chromatin functional domains reveals novel synergisms among distinct heterochromatin components. *Mol. Cell. Proteomics*, **12**, 764–780.
28. Soldi,M., Mari,T., Nicosia,L., Musiani,D., Sigismondo,G., Cuomo,A., Pavesi,G. and Bonaldi,T. (2017) Chromatin proteomics reveals novel combinatorial histone modification signatures that mark distinct subpopulations of macrophage enhancers. *Nucleic Acids Res.*, **45**, 12195–12213.
29. Ong,S.E., Blagoev,B., Kratchmarova,I., Kristensen,D.B., Steen,H., Pandey,A. and Mann,M. (2002) Stable isotope labeling by amino acids in cell culture, SILAC, as a simple and accurate approach to expression proteomics. *Mol. Cell. Proteomics*, **1**, 376–386.
30. Hughes,C.S., Foehr,S., Garfield,D.A., Furlong,E.E., Steinmetz,L.M. and Krijgsveld,J. (2014) Ultrasensitive proteome analysis using paramagnetic bead technology. *Mol. Syst. Biol.*, **10**, 757.

31. Hughes,C.S., Moggridge,S., Muller,T., Sorensen,P.H., Morin,G.B. and Krijgsveld,J. (2019) Single-pot, solid-phase-enhanced sample preparation for proteomics experiments. *Nat. Protoc.*, **14**, 68–85.

32. Rappsilber,J., Ishihama,Y. and Mann,M. (2003) Stop and go extraction tips for matrix-assisted laser desorption/ionization, nanoelectrospray, and LC/MS sample pretreatment in proteomics. *Anal. Chem.*, **75**, 663–670.

33. Cox,J. and Mann,M. (2008) MaxQuant enables high peptide identification rates, individualized p.p.b.-range mass accuracies and proteome-wide protein quantification. *Nat. Biotechnol.*, **26**, 1367–1372.

34. Tyanova,S., Temu,T. and Cox,J. (2016) The MaxQuant computational platform for mass spectrometry-based shotgun proteomics. *Nat. Protoc.*, **11**, 2301–2319.

35. Zhou,Y., Zhou,B., Pache,L., Chang,M., Khodabakhshi,A.H., Tanaseichuk,O., Benner,C. and Chanda,S.K. (2019) Metascape provides a biologist-oriented resource for the analysis of systems-level datasets. *Nat. Commun.*, **10**, 1523.

36. Aymard,F., Bugler,B., Schmidt,C.K., Guillou,E., Caron,P., Briois,S., Iacovoni,J.S., Daburon,V., Miller,K.M., Jackson,S.P. *et al.* (2014) Transcriptionally active chromatin recruits homologous recombination at DNA double-strand breaks. *Nat. Struct. Mol. Biol.*, **21**, 366–374.

37. Khoury-Haddad,H., Guttmann-Raviv,N., Ipenberg,I., Huggins,D., Jeyasekharan,A.D. and Ayoub,N. (2014) PARP1-dependent recruitment of KDM4D histone demethylase to DNA damage sites promotes double-strand break repair. *Proc. Natl. Acad. Sci. U.S.A.*, **111**, E728–E737.

38. Certo,M.T., Ryu,B.Y., Annis,J.E., Garibov,M., Jarjour,J., Rawlings,D.J. and Scharenberg,A.M. (2011) Tracking genome engineering outcome at individual DNA breakpoints. *Nat. Methods*, **8**, 671–676.

39. Abu-Zhayia,E.R., Khoury-Haddad,H., Guttmann-Raviv,N., Serruya,R., Jarrous,N. and Ayoub,N. (2017) A role of human rnase P subunits, Rpp29 and Rpp21, in homology directed-repair of double-strand breaks. *Sci. Rep.*, **7**, 1002.

40. Lund-Andersen,C., Patzke,S., Nahse-Kumpf,V. and Syljuasen,R.G. (2014) PLK1-inhibition can cause radiosensitization or radioresistance dependent on the treatment schedule. *Radiother. Oncol.*, **110**, 355–361.

41. Franken,N.A., Rodermond,H.M., Stap,J., Haveman,J. and van Bree,C. (2006) Clonogenic assay of cells in vitro. *Nat. Protoc.*, **1**, 2315–2319.

42. Perez-Riverol,Y., Csordas,A., Bai,J., Bernal-Llinares,M., Hewapathirana,S., Kundu,D.J., Inuganti,A., Griss,J., Mayer,G., Eisenacher,M. *et al.* (2019) The PRIDE database and related tools and resources in 2019: improving support for quantification data. *Nucleic Acids Res.*, **47**, D442–D450.

43. Hilger,M. and Mann,M. (2012) Triple SILAC to determine stimulus specific interactions in the Wnt pathway. *J. Proteome Res.*, **11**, 982–994.

44. Palmieri,D., Valentino,T., D'Angelo,D., De Martino,I., Postiglione,I., Pacelli,R., Croce,C.M., Fedele,M. and Fusco,A. (2011) HMGA proteins promote ATM expression and enhance cancer cell resistance to genotoxic agents. *Oncogene*, **30**, 3024–3035.

45. Qi,W., Wang,R., Chen,H., Wang,X., Xiao,T., Boldogh,I., Ba,X., Han,L. and Zeng,X. (2015) BRG1 promotes the repair of DNA double-strand breaks by facilitating the replacement of RPA with RAD51. *J. Cell Sci.*, **128**, 317–330.

46. Tacke,R., Tohyama,M., Ogawa,S. and Manley,J.L. (1998) Human Tra2 proteins are sequence-specific activators of pre-mRNA splicing. *Cell*, **93**, 139–148.

47. Vidi,P.A., Liu,J., Salles,D., Jayaraman,S., Dorfman,G., Gray,M., Abad,P., Moghe,P.V., Irudayaraj,J.M., Wiesmuller,L. *et al.* (2014) NuMA promotes homologous recombination repair by regulating the accumulation of the ISWI atpase SNF2h at DNA breaks. *Nucleic Acids Res.*, **42**, 6365–6379.

48. Moreno,N.S., Liu,J., Haas,K.M., Parker,L.L., Chakraborty,C., Kron,S.J., Hodges,K., Miller,L.D., Langefeld,C., Robinson,P.J. *et al.* (2019) The nuclear structural protein NuMA is a negative regulator of 53BP1 in DNA double-strand break repair. *Nucleic Acids Res.*, **47**, 10475.

49. Onyango,D.O., Lee,G. and Stark,J.M. (2017) PRPF8 is important for BRCA1-mediated homologous recombination. *OncoTargets Ther.*, **8**, 93319–93337.

50. Rogakou,E.P., Pilch,D.R., Orr,A.H., Ivanova,V.S. and Bonner,W.M. (1998) DNA double-stranded breaks induce histone H2AX phosphorylation on serine 139. *J. Biol. Chem.*, **273**, 5858–5868.

51. Kleiner,R.E., Verma,P., Molloy,K.R., Chait,B.T. and Kapoor,T.M. (2015) Chemical proteomics reveals a gammaH2AX-53BP1 interaction in the DNA damage response. *Nat. Chem. Biol.*, **11**, 807–814.

52. Cremona,C.A., Sarangi,P., Yang,Y., Hang,L.E., Rahman,S. and Zhao,X. (2012) Extensive DNA damage-induced sumoylation contributes to replication and repair and acts in addition to the mec1 checkpoint. *Mol. Cell*, **45**, 422–432.

53. Francia,S., Michelini,F., Saxena,A., Tang,D., de Hoon,M., Anelli,V., Mione,M., Carninci,P. and d'Adda di Fagagna,F. (2012) Site-specific DICER and DROSHA RNA products control the DNA-damage response. *Nature*, **488**, 231–235.

54. Beli,P., Lukashchuk,N., Wagner,S.A., Weinert,B.T., Olsen,J.V., Baskcomb,L., Mann,M., Jackson,S.P. and Choudhary,C. (2012) Proteomic investigations reveal a role for RNA processing factor THRAP3 in the DNA damage response. *Mol. Cell*, **46**, 212–225.

55. Kang,H.J., Eom,H.J., Kim,H., Myung,K., Kwon,H.M. and Choi,J.H. (2021) Thrap3 promotes R-loop resolution via interaction with methylated DDX5. *Exp. Mol. Med.*, **53**, 1602–1611.

56. Song,C., Hotz-Wagenblatt,A., Voit,R. and Grummt,I. (2017) SIRT7 and the DEAD-box helicase DDX21 cooperate to resolve genomic R loops and safeguard genome stability. *Genes Dev.*, **31**, 1370–1381.

57. Tian,T., Bu,M., Chen,X., Ding,L., Yang,Y., Han,J., Feng,X.H., Xu,P., Liu,T., Ying,S. *et al.* (2021) The ZATT-TOP2A-PICH axis drives extensive replication fork reversal to promote genome stability. *Mol. Cell*, **81**, 198–211.

58. Neumayer,G., Helfricht,A., Shim,S.Y., Le,H.T., Lundin,C., Belzil,C., Chansard,M., Yu,Y., Lees-Miller,S.P., Gruss,O.J. *et al.* (2012) Targeting protein for xenopus kinesin-like protein 2 (TPX2) regulates gamma-histone 2AX (gamma-H2AX) levels upon ionizing radiation. *J. Biol. Chem.*, **287**, 42206–42222.

59. Byrum,A.K., Carvajal-Maldonado,D., Mudge,M.C., Valle-Garcia,D., Majid,M.C., Patel,R., Sowa,M.E., Gygi,S.P., Harper,J.W., Shi,Y. *et al.* (2019) Mitotic regulators TPX2 and Aurora A protect DNA during replication stress by counteracting 53BP1 function. *J. Cell Biol.*, **218**, 422–432.

60. Koo,S.J., Fernandez-Montalvan,A.E., Badock,V., Ott,C.J., Holton,S.J., von Ahsen,O., Toedling,J., Vittori,S., Bradner,J.E. and Gorjanacz,M. (2016) ATAD2 is an epigenetic reader of newly synthesized histone marks during DNA replication. *OncoTargets Ther.*, **7**, 70323–70335.

61. Ciro,M., Prosperini,E., Quarto,M., Grazini,U., Walfridsson,J., McBlane,F., Nucifero,P., Pacchiana,G., Capra,M., Christensen,J. *et al.* (2009) ATAD2 is a novel cofactor for MYC, overexpressed and amplified in aggressive tumors. *Cancer Res.*, **69**, 8491–8498.

62. Duan,Z., Andrews,N.P., Chen,C.Z., Fan,M., Wang,J., Shen,J., Li,J.J. and Chen,H.W. (2020) Targeting bromodomain protein ANCCA/ATAD2 enhances the efficacy of dnadamaging chemotherapy agents and radiation. *Oncol. Rep.*, **43**, 318–327.

63. Kliszczak,A.E., Rainey,M.D., Harhen,B., Boisvert,F.M. and Santocanale,C. (2011) DNA mediated chromatin pull-down for the study of chromatin replication. *Sci. Rep.*, **1**, 95.

64. Sirbu,B.M., Couch,F.B., Feigerle,J.T., Bhaskara,S., Hiebert,S.W. and Cortez,D. (2011) Analysis of protein dynamics at active, stalled, and collapsed replication forks. *Genes Dev.*, **25**, 1320–1327.

65. Bao,X., Guo,X., Yin,M., Tariq,M., Lai,Y., Kanwal,S., Zhou,J., Li,N., Lv,Y., Pulido-Quetglas,C. *et al.* (2018) Capturing the interactome of newly transcribed RNA. *Nat. Methods*, **15**, 213–220.

66. Aranda,S., Alcaine-Colet,A., Blanco,E., Borras,E., Caillot,C., Sabido,E. and Di Croce,L. (2019) Chromatin capture links the metabolic enzyme AHCY to stem cell proliferation. *Sci. Adv.*, **5**, eaav2448.

67. Alabert,C., Bukowski-Wills,J.C., Lee,S.B., Kustatscher,G., Nakamura,K., de Lima Alves,F., Menard,P., Mejlvang,J., Rappsilber,J. and Groth,A. (2014) Nascent chromatin capture proteomics determines chromatin dynamics during DNA replication and identifies unknown fork components. *Nat. Cell Biol.*, **16**, 281–293.

68. Nakamura,K., Kustatscher,G., Alabert,C., Hodl,M., Forne,I., Volker-Albert,M., Satpathy,S., Beyer,T.E., Mailand,N., Choudhary,C. *et al.* (2021) Proteome dynamics at broken replication forks reveal a distinct ATM-directed repair response suppressing DNA double-strand break ubiquitination. *Mol. Cell*, **81**, 1084–1099.

69. Cheblal,A., Challa,K., Seeber,A., Shimada,K., Yoshida,H., Ferreira,H.C., Amitai,A. and Gasser,S.M. (2020) DNA damage-Induced nucleosome depletion enhances homology search independently of local break movement. *Mol. Cell*, **80**, 311–326.

70. Zhang,L., Huang,Q., Lou,J., Zou,L., Wang,Y., Zhang,P., Yang,G., Zhang,J., Yu,L., Yan,D. *et al.* (2017) A novel PHD-finger protein 14/KIF4A complex overexpressed in lung cancer is involved in cell mitosis regulation and tumorigenesis. *OncoTargets Ther.*, **8**, 19684–19698.

71. Karagoz,K., Mehta,G.A., Khella,C.A., Khanna,P. and Gatza,M.L. (2019) Integrative proteogenomic analyses of human tumours identifies ADNP as a novel oncogenic mediator of cell cycle progression in high-grade serous ovarian cancer with poor prognosis. *EBioMedicine*, **50**, 191–202.

72. Barak,O., Lazzaro,M.A., Lane,W.S., Speicher,D.W., Picketts,D.J. and Shiekhattar,R. (2003) Isolation of human NURF: a regulator of engrailed gene expression. *EMBO J.*, **22**, 6089–6100.

73. Kaaij,L.J.T., Mohn,F., van der Weide,R.H., de Wit,E. and Buhler,M. (2019) The ChAHP complex counteracts chromatin looping at CTCF sites that emerged from SINE expansions in mouse. *Cell*, **178**, 1437–1451.

74. Pan,G.Z., Zhang,K., Geng,S.J., Lan,C., Hu,X., Li,C.H., Ji,H.Y., Li,C.Y., Hu,X.S., Wang,Y. *et al.* (2022) PHF14 knockdown causes apoptosis by inducing DNA damage and the of the in colorectal cancer. *Cancer Lett.*, **531**, 109–123.

75. Gong,F. and Miller,K.M. (2019) Histone methylation and the DNA damage response. *Mutat. Res.*, **780**, 37–47.

76. Suka,N., Suka,Y., Carmen,A.A., Wu,J. and Grunstein,M. (2001) Highly specific antibodies determine histone acetylation site usage in yeast heterochromatin and euchromatin. *Mol. Cell*, **8**, 473–479.

77. Houston,S.I., McManus,K.J., Adams,M.M., Sims,J.K., Carpenter,P.B., Hendzel,M.J. and Rice,J.C. (2008) Catalytic function of the PR-Set7 histone H4 lysine 20 monomethyltransferase is essential for mitotic entry and genomic stability. *J. Biol. Chem.*, **283**, 19478–19488.

78. Oda,H., Hubner,M.R., Beck,D.B., Vermeulen,M., Hurwitz,J., Spector,D.L. and Reinberg,D. (2010) Regulation of the histone H4 monomethylase PR-Set7 by CRL4(Cdt2)-mediated PCNA-dependent degradation during DNA damage. *Mol. Cell*, **40**, 364–376.

79. Huyen,Y., Zgheib,O., Ditullio,R.A. Jr., Gorgoulis,V.G., Zacharatos,P., Petty,T.J., Sheston,E.A., Mellert,H.S., Stavridi,E.S. and Halazonetis,T.D. (2004) Methylated lysine 79 of histone H3 targets 53BP1 to DNA double-strand breaks. *Nature*, **432**, 406–411.

80. Schubeler,D., MacAlpine,D.M., Scalzo,D., Wirbelauer,C., Kooperberg,C., van Leeuwen,F., Gottschling,D.E., O'Neill,L.P., Turner,B.M., Delrow,J. *et al.* (2004) The histone modification pattern of active genes revealed through genome-wide chromatin analysis of a higher eukaryote. *Genes Dev.*, **18**, 1263–1271.

81. Tweedie-Cullen,R.Y., Brunner,A.M., Grossmann,J., Mohanna,S., Sichau,D., Nanni,P., Panse,C. and Mansuy,I.M. (2012) Identification of combinatorial patterns of post-translational modifications on individual histones in the mouse brain. *PLoS One*, **7**, e36980.

82. Fenley,A.T., Anandakrishnan,R., Kidane,Y.H. and Onufriev,A.V. (2018) Modulation of nucleosomal DNA accessibility via charge-altering post-translational modifications in histone core. *Epigenetics Chromatin*, **11**, 11.

83. Crosetto,N., Mitra,A., Silva,M.J., Bienko,M., Dojer,N., Wang,Q., Karaca,E., Chiarle,R., Skrzypczak,M., Ginalski,K. *et al.* (2013) Nucleotide-resolution DNA double-strand break mapping by next-generation sequencing. *Nat. Methods*, **10**, 361–365.

84. Zee,B.M., Levin,R.S., Xu,B., LeRoy,G., Wingreen,N.S. and Garcia,B.A. (2010) In vivo residue-specific histone methylation dynamics. *J. Biol. Chem.*, **285**, 3341–3350.

85. Di Cerbo,V., Mohn,F., Ryan,D.P., Montellier,E., Kacem,S., Tropberger,P., Kallis,E., Holzner,M., Hoerner,L., Feldmann,A. *et al.* (2014) Acetylation of histone H3 at lysine 64 regulates nucleosome dynamics and facilitates transcription. *Elife*, **3**, e01632.

86. Yang,Q., Zhu,Q., Lu,X., Du,Y., Cao,L., Shen,C., Hou,T., Li,M., Li,Z., Liu,C. *et al.* (2017) G9a coordinates with the RPA complex to promote DNA damage repair and cell survival. *Proc. Natl. Acad. Sci. U.S.A.*, **114**, E6054–E6063.

87. Ginjala,V., Rodriguez-Colon,L., Ganguly,B., Gangidi,P., Gallina,P., Al-Hraishawi,H., Kulkarni,A., Tang,J., Gheeya,J., Simhadri,S. *et al.* (2017) Protein-lysine methyltransferases G9a and GLP1 promote responses to DNA damage. *Sci. Rep.*, **7**, 16613.

88. Chen,C.C., Carson,J.J., Feser,J., Tamburini,B., Zabaronick,S., Linger,J. and Tyler,J.K. (2008) Acetylated lysine 56 on histone H3 drives chromatin assembly after repair and signals for the completion of repair. *Cell*, **134**, 231–243.

89. Yu,Y., Song,C., Zhang,Q., DiMaggio,P.A., Garcia,B.A., York,A., Carey,M.F. and Grunstein,M. (2012) Histone H3 lysine 56 methylation regulates DNA replication through its interaction with PCNA. *Mol. Cell*, **46**, 7–17.

90. Agarwal,P. and Jackson,S.P. (2016) G9a inhibition potentiates the anti-tumour activity of DNA double-strand break inducing agents by impairing DNA repair independent of p53 status. *Cancer Lett.*, **380**, 467–475.

91. Sirbu,B.M., Couch,F.B. and Cortez,D. (2012) Monitoring the spatiotemporal dynamics of proteins at replication forks and in assembled chromatin using isolation of proteins on nascent DNA. *Nat. Protoc.*, **7**, 594–605.

92. Moyal,L., Lerenthal,Y., Gana-Weisz,M., Mass,G., So,S., Wang,S.Y., Eppink,B., Chung,Y.M., Shalev,G., Shema,E. *et al.* (2011) Requirement of ATM-dependent monoubiquitylation of histone H2B for timely repair of DNA double-strand breaks. *Mol. Cell*, **41**, 529–542.

93. Masumoto,H., Hawke,D., Kobayashi,R. and Verreault,A. (2005) A role for cell-cycle-regulated histone H3 lysine 56 acetylation in the DNA damage response. *Nature*, **436**, 294–298.

94. Mirza,M.R., Monk,B.J., Herrstedt,J., Oza,A.M., Mahner,S., Redondo,A., Fabbro,M., Ledermann,J.A., Lorusso,D., Vergote,I. *et al.* (2016) Niraparib maintenance therapy in platinum-Sensitive, recurrent ovarian cancer. *N. Engl. J. Med.*, **375**, 2154–2164.

95. Coleman,R.L., Oza,A.M., Lorusso,D., Aghajanian,C., Oaknin,A., Dean,A., Colombo,N., Weberpals,J.I., Clamp,A., Scambia,G. *et al.* (2017) Rucaparib maintenance treatment for recurrent ovarian carcinoma after response to platinum therapy (ARIEL3): a randomised, double-blind, placebo-controlled, phase 3 trial. *Lancet*, **390**, 1949–1961.

96. Pfister,S.X. and Ashworth,A. (2017) Marked for death: targeting epigenetic changes in cancer. *Nat. Rev. Drug Discov.*, **16**, 241–263.

97. Ito,T., Young,M.J., Li,R., Jain,S., Wernitznig,A., Krill-Burger,J.M., Lemke,C.T., Monducci,D., Rodriguez,D.J., Chang,L. *et al.* (2021) Paralog knockout profiling identifies DUSP4 and DUSP6 as a digenic dependence in MAPK pathway-driven cancers. *Nat. Genet.*, **53**, 1664–1672.

98. Elia,A.E., Boardman,A.P., Wang,D.C., Huttlin,E.L., Everley,R.A., Dephoure,N., Zhou,C., Koren,I., Gygi,S.P. and Elledge,S.J. (2015) Quantitative proteomic atlas of ubiquitination and acetylation in the DNA damage response. *Mol. Cell*, **59**, 867–881.

99. Zijlmans,D.W., Talon,I., Verhelst,S., Bendall,A., Van Nerum,K., Javali,A., Malcolm,A.A., van Knippenberg,S., Biggins,L., To,S.K. *et al.* (2022) Integrated multi-omics reveal polycomb repressive complex 2 restricts human trophoblast induction. *Nat. Cell Biol.*, **24**, 858–871.